JFM PAPERS

The influence of free stream turbulence on the development of a wind turbine wake

Stefano Gambuzza[1],† **and Bharathram Ganapathisubramani**[1]

[1] Aerodynamics and Flight Mechanics Research Group, University of Southampton, Southampton SO17 1BJ, UK

The wake of an isolated model-scale wind turbine is analysed in a set of inflow conditions having free stream turbulence intensity between 3 % and 12 %, and integral time scales in the range of 0.1–10 times the convective time scale based on the turbine diameter. It is observed that the wake generated by the turbine evolves more rapidly, with the onset of the wake evolution being closer to the turbine, for high turbulence intensity and low integral time scale flows, in accordance with literature, while flows at higher integral time scales result in a slow wake evolution, akin to that generated by low-turbulence inflow conditions despite the highly turbulent ambient condition. The delayed onset of the wake evolution is connected to the stability of the shear layer enveloping the near-wake, which is favoured for low-turbulence or high-integral time scale flows, and to the stability of the helical vortex set surrounding the wake, as this favours interaction events and prevents momentum exchange at the wake boundary which hinder wake evolution. The rate at which the velocity in the wake recovers to undisturbed conditions is instead analytically shown to be a function of the Reynolds shear stress at the wake centreline, an observation that is confirmed by measurements. The rate of production of Reynolds shear stress in the wake is then connected to the power harvested by the turbine to explain the differences between flows at equivalent turbulence intensity and different integral time scales. The wake recovery rate, and by extension the behaviour of the turbine wake in high-integral time scale flows, is seen to be a linear function of the free stream turbulence intensity for flows with Kolmogorov-like turbulence spectrum, in accordance with literature. This relation is seen not to hold for flows with different free stream turbulence spectral distribution; however, this trend is recovered if the contributions of low frequency velocity components to the turbulence intensity are ignored or filtered out from the computation.

Key words: wakes

---

† Email address for correspondence: s.gambuzza@soton.ac.uk

963 A19-1

1. Introduction

Wind turbines are machines that present a number of peculiar characteristics regarding their operation: first, these are situated in the lowermost portion of the atmospheric boundary layer, and thus harvest power from turbulent, sheared inflows. Moreover, to accommodate for the rising market demand in renewable energy, these are often grouped in wind farms that house a large number of these machines in a finite area: as a result, all turbines that are not situated in the first row of the wind farm experience, as incoming flow, a combination of the wakes of upstream machines and turbulent free stream entrained from the atmospheric boundary layer surrounding the farm. In particular, the presence of upstream machines limits the power that a wind turbine in the back rows of a farm can harvest, as it will harvest energy from a lower-momentum inflow (Frandsen & Barthelmie 2002; Barthelmie & Jensen 2010). For this reason, a good knowledge of the wake generated by a wind turbine in a complex, turbulent inflow is paramount to the prolonged development and deployment of wind energy around the world.

As mentioned, the environment in which wind turbines operate is turbulent and sheared: this is often parametrised with the free stream turbulence intensity, defined as

$$I_\infty = \frac{\sqrt{\overline{u'^2}}}{U_\infty}, \tag{1.1}$$

where U_∞ is the bulk free stream speed, and $\sqrt{\overline{u'^2}}$ is the standard deviation of the velocity time-history. Elliott & Cadogan (1990) report data showing that turbines in an on-shore environment are subject to $I_\infty < 15\%$ for 95 % of their operating life. Similarly, Wagner *et al.* (2011) and Peña *et al.* (2016) report that turbines at the Høvsøre on-shore testing site experience values of I_∞ between 2 % and 14 %, with a strong dependency on the wind direction: less turbulent inflows are observed for winds arising from the ocean. Turbulence intensity for offshore sites is usually lower, with values of I_∞ comprised between 6 % and 8 % (Barthelmie *et al.* 2005; Türk & Emeis 2010).

Wakes of wind turbines are complex in nature, being characterised by the superposition of a large number of events: in the simplest of descriptions, the time-averaged wake of a wind turbine is, sufficiently far from the turbine rotor, characterised by a self-similar velocity deficit profile having a Gaussian distribution in the stream-normal directions (Medici & Alfredsson 2006); this is in line with the wakes generated by other axisymmetric bluff bodies such as spheres (Uberoi & Freymuth 1970) or porous plates (Rind & Castro 2012a; Aubrun *et al.* 2019; Vinnes *et al.* 2022). Closer to the turbine, the actual shape of the velocity profile is dominated by the distribution of pressure around the turbine blades: although sometimes the velocity deficit distribution is constant along a radial direction (Medici & Alfredsson 2006; Mycek *et al.* 2014; Lignarolo *et al.* 2015), this need not necessarily be, especially for turbines that are not operating at on-design conditions (Vermeer, Sørensen & Crespo 2003; Carbajo Fuertes, Markfort & Porté-Agel 2018; Foti *et al.* 2018; Dasari *et al.* 2019). The transition from these arbitrary profiles to the self-similar Gaussian ones is understood to be a function of the free stream turbulence intensity (Medici & Alfredsson 2006; Ishihara & Qian 2018). This region of lower velocity is separated from the surrounding free stream by an annular shear layer which is dominated by the presence of a helical vortex structure (Lissaman 1979; Crespo & Hernández 1996; Troldborg, Sorensen & Mikkelsen 2010; De Cillis *et al.* 2020): this is analogous to the classical horseshoe vortex characteristic of finite wings generating lift, and it takes a helical structure due to the rotation of the blades as free stream convects these vortices downstream. The stability of this structure has been connected

to the onset of wake evolution (Lignarolo *et al.* 2014, 2015), where a strong shear layer enveloping the wake inhibits it; moreover, the stability (or lack thereof) is also seen to drive a low-frequency motion of the wake in the stream-normal directions, named wake meandering (Medici & Alfredsson 2006; Heisel, Hong & Guala 2018; De Cillis *et al.* 2020), with this motion being favoured by unstable shear layers. In general, an increase in the free stream turbulence intensity is seen to hasten the transition to a self-similar velocity profile (Medici & Alfredsson 2006) and a smaller velocity deficit at a given distance from the turbine (Christiansen & Hasager 2005; Chamorro, Arndt & Sotiropoulos 2012; Bastankhah & Porté-Agel 2014); this is seen from the point of view of a wind farm operator as a larger distance necessary between turbines in an offshore environment, as the lower free stream turbulence intensity of those sites does not favour wake recovery as much as in on-shore sites (Christiansen & Hasager 2005). The stability of the shear layer is also seen to be related to the free stream turbulence intensity, shown by Sørensen *et al.* (2015) as a relationship between the breakdown of the helical vortex structure and I_∞.

Often, the wake generated by the turbine is divided into a near- and a far-wake region, with the former being characterised by the presence of the helical vortex structure and a non-self-similar velocity profile, while the latter shows opposite characteristics. The division of the wake into a near and far field is commonplace for wakes generated by all bluff bodies, and goes back to the first works by Castro (1971) and Pope & Whitelaw (1976). Attempts to define the location of the boundary between the near- and the far-wake have been, in recent times, published by a number of authors: for instance, Sørensen *et al.* (2015) defines the boundary as the point of inflection of the turbulent kinetic energy content of some selected proper-orthogonal-decomposition (POD) modes in the turbine wake. De Cillis *et al.* (2020) instead defines the boundary to be the location for which the time-averaged turbulent kinetic energy in the wake falls below a given threshold. Wu & Porté-Agel (2012) uses instead the change in sign in the turbulent kinetic energy advection term. Authors such as Howard *et al.* (2015) and Kang, Yang & Sotiropoulos (2014) instead connect the onset of wake meandering to the transition from near- to far-wake: Kang *et al.* (2014) show, from large-eddy simulation (LES) around a turbine, that the root-vortex set undergoes instability, starting meandering in the near-wake; as this motion reaches the annular shear layer around the turbine, it favours its breakdown and the full transition to a far-wake, which is confirmed by the experiments of Howard *et al.* (2015). Similar results are shown by Foti *et al.* (2018). Neunaber *et al.* (2020) instead proposes a more complex definition of the turbine wake, which places two intermediate regions, named transition and decay regions, between the near- and far-wake; according to the authors, the near-wake is characterised by the presence of homogeneous and isotropic turbulence at its centre, unlike the other regions where the nacelle influence is still observed on the turbulence statistics. In all cases, transition to the far-wake is hastened by a more turbulent free stream. It can be understood that, given the differences between these methods, the location of the transition each model gives is different from that of any other model. This is to be expected as near- and far-wake are terms that describe the absence or presence of a large set of events, which need not appear or disappear simultaneously; as such, the distinction between near- and far-wake, and the estimation of this transition can only be qualitative.

It can be understood that not all these phenomena in the wake are of interest to a wind turbine operator: for this reason, engineering applications usually treat the wake statistically in a simplified form, often ignoring some of the aspects here described. Analytical wake models are engineering tools often used to predict the wake generated by wind turbines; these often relate the flow velocity in the turbine wake to some global parameters, simple to measure or estimate. The model that has seen the most widespread

use in the literature recently is the Gaussian wake model (Bastankhah & Porté-Agel 2014): according to this, one has that the velocity deficit in the turbine wake is given by

$$\frac{\Delta U}{U_\infty} = \frac{U_\infty - U}{U_\infty} = \left(1 - \sqrt{1 - \frac{C_T}{8(\sigma_w/D)^2}}\right) \exp\left(-\frac{1}{2(\sigma_w/D)^2}\left(\frac{r}{D}\right)^2\right), \qquad (1.2)$$

$$\frac{\sigma_w}{D} = \epsilon + k^*\frac{x}{D}, \qquad (1.3)$$

where U_∞ is the free stream speed, U is the velocity in the wake function of the streamwise distance from the turbine x and the radial distance away from the turbine axis r, D is the turbine radius, C_T is the thrust coefficient, ϵ is a known function of C_T and k^* is a parameter related to the spatial growth of the wake. The effect of turbulence, which has been seen to be for other bluff-bodies that of hastening the wake development and shortening the wake, is often represented as a change in the wake recovery rate k^*. Niayifar & Porté-Agel (2016) report an elaboration of LES data of the wake generated by a commercial turbine, showing a linear relationship between the free stream turbulence intensity and the wake recovery rate, for a constant value of C_T; this is also observed by Carbajo Fuertes *et al.* (2018) with field data on the wake of a turbine acquired with light detection and ranging (LiDAR). For the similar Jensen wake model (Jensen 1983), Peña *et al.* (2016) show that the wake recovery rate is a linear function of the free stream turbulence intensity if one assumes an inflow that is modelled with Monin–Obukhov similarity theory (Monin & Obukhov 1954). However, some works in recent literature have outlined how the predictions of wake models can be better tuned by introducing one additional parameter: for instance, Neunaber, Peinke & Obligado (2022) shows that the accuracy of the predictions of commonly used wake models can be improved by introducing a virtual origin in their equations. This practice, commonplace when treating wakes of bluff bodies, is seldom carried out in wind engineering. In this work, the authors measure the wakes of two model-scale wind turbines, subject to either a laminar inflow or to the wake of an upstream machine. Their data show that the addition of a virtual origin in analytical wake models can improve the quality of the predictions for the wake of downstream machines, hinting to the conclusion that a virtual origin might include information on the inflow conditions. However, data included in their paper only consist of the wakes generated under either a laminar inflow or the wake of another turbine: given the large range of turbulent flows that turbines experience, it is important to observe whether a virtual origin can improve on the predictions of analytical wake models for an arbitrary inflow condition, and what is its physical meaning. While a large body of literature has been dedicated to understanding the effects of free stream turbulence intensity on the wake and on analytical prediction, little has been done to characterise the wake developed by a turbine in the presence of flows with different spectral content of turbulence. It is well established that the distribution of inflow turbulence affects the near-wake and the power a wind turbine generates (Sheinman & Rosen 1992; Chamorro *et al.* 2015; Tobin, Zhu & Chamorro 2015; Deskos, Payne & Gaurier 2020; Li *et al.* 2020; Gambuzza & Ganapathisubramani 2021) and the drag generated by turbine simulators (Blackmore *et al.* 2014), with turbines being more apt at converting velocity fluctuations into power if those are present as lower-frequency contributions. Most works in the literature therefore highlight how a wind turbine acts as a low-pass filter when converting inflow into mechanical power. It can thus be assumed that the wake generated by a turbine in flows with different representations in the frequency domain are characterised by different scales, and indeed some works report different spectral composition between the free stream and the wake generated by the turbines (Heisel *et al.* 2018;

Tobin & Chamorro 2019). In addition, Chatterjee & Peet (2018, 2021) show that, from LES of an infinite wind farm, the mechanism of mean kinetic energy entrainment from the free stream to the wake is favoured in the presence of very-large-scale structures, with sizes of approximately 10 times the turbine diameter. Their work shows that the presence of a turbine effectively remodulates the spectral content of the wake, favouring large-scale motions in the wake. Whether this leads to different mechanisms of wake development is an assumption that has seldom been tested in the literature for an isolated turbine, and indeed engineering models do assume no effect of the turbulence spectrum on the wake evolution, with parameters such as k^* being only a function of I_∞. For this reason, this paper aims to investigate the relationship between the changing inflow conditions to which a turbine is subject and the mechanisms that regulate and dominate the development of this wake. We follow on from our previous work in Gambuzza & Ganapathisubramani (2021) and carry out an experimental study to characterise the wake of a model-scale turbine under different inflow turbulence conditions.

This paper is structured as follows: § 2 will briefly present the experimental methodology used to collect the data here presented, along with its shortcomings. Section 3 will present the results obtained: this chapter is further divided into three subsections, which will relate more in detail to the predictions of engineering models (§ 3.1) and to the physics behind the trends observed (§§ 3.2 and 3.3). Section 4 will summarise these findings concisely.

2. Experimental method

This paper reports the measurements of velocity in the wake of a model-scale wind turbine, measured via planar particle image velocimetry (PIV) in a wind tunnel equipped with an active turbulence generating grid. This section will expand on the experimental methodology that has been employed to obtain the results reported in the remainder of the paper, outlining the main characteristics and the limitations of the techniques employed. Some of the techniques used in this study are described in more detail in a previous study by Gambuzza & Ganapathisubramani (2021).

2.1. *Facility*

The experiments were carried out in the 3×2 boundary layer wind tunnel at the University of Southampton. This is a suction wind tunnel having a rectangular cross-section of size $0.9 \times 0.6 \, \text{m}^2$, and a total usable length of constant cross-section of 4.5 m. Flow is driven by a fan placed downstream of the test section, and flow conditioning is carried out by a set of honeycomb meshes upstream of a contraction that leads to the test section. During the tests here described, the wind tunnel has been equipped with a turbulence-generating active grid, designed to the specifications of Makita (1991), which is able to generate turbulent flows with different levels of shear and free stream turbulence intensities up to 16 % (Hearst & Ganapathisubramani 2017; Li *et al.* 2020); no shear has been generated for the measurements presented in this study. This grid is composed of 18 stepper motors that independently drive 11 vertical rods and 7 horizontal rods, each moving a set of agitator wings. The mesh spacing between rods M is 81 mm. The grid is operated by changing the angular velocity of each rod to a random value in a predetermined interval, with rods allowed to cruise to speed for a limited time before changing direction and speed: this actuation procedure is described in detail by Poorte & Biesheuvel (2002) as the double-random mode. The active grid is situated at the inlet of the wind tunnel test section, with the rods covering the whole of the wind tunnel cross-section.

r/r_{tip}	c/r_{tip}	β (deg)	Aerofoil
0.13	0.13	58.20	NACA 63-418
0.20	0.27	35.58	NACA 63-418
0.30	0.26	24.13	NACA 63-418
0.40	0.24	16.76	NACA 63-418
0.50	0.22	11.77	NACA 63-418
0.60	0.21	8.22	NACA 63-418
0.70	0.19	5.58	NACA 63-418
0.80	0.17	3.55	NACA 63-418
0.90	0.16	1.94	NACA 63-418
1.00	0.14	0.64	NACA 63-418

Table 1. Turbine geometry, defined as the distribution of chord c, twist β and aerofoil shape along the blade span coordinate r.

During the tests, the wind tunnel fan was operated to generate a mean free stream speed U_∞ equal to $8\,\mathrm{m\,s^{-1}}$. This was measured by means of a Pitot probe placed $2.5M$ upstream of the active grid. To account for the change in U_∞ along the test section, this was calibrated to a Pitot placed at the same location as the turbine in an otherwise empty test section.

2.2. *Model-scale turbine*

The turbine used during these tests is a speed controlled, fixed pitch model-scale wind turbine, having a rotor of diameter D equal to $0.18\,\mathrm{m}$. For this value of D and the aforementioned constant value of U_∞, the diameter-based Reynolds number of these tests is $Re = 9.6 \times 10^4$. Data reported by Chamorro *et al.* (2012) show that this is sufficiently high to attain Reynolds-independent results both in the mean and the second moment of the wake velocity signals. The turbine rotor has been directly connected to a brushed permanent magnet DC machine that was used as a generator to brake the rotor while operating. This was not connected to other sources of mechanical or electrical power, with the only torque acting on the turbine shaft being the one generated by the free stream on the turbine blades, and the power generated being transformed into heat dissipated by the motor. The turbine nacelle was supported by an aluminium mast of diameter $15.75\,\mathrm{mm}$, which placed the centre of the rotor at the centre of the test section. The turbine was then located at a streamwise distance of $36M = 16D$ downstream of the active grid. The geometry of the blade, defined as the distribution of chord and twist along the blade span, is reported in table 1, where $r_{tip} = D/2$ is the spanwise location of the last section of the blade. The turbine blade is designed to harvest maximum power from the incoming flow at a tip-speed ratio λ of 4; this parameter is defined as

$$\lambda = \frac{\omega\, r_{tip}}{U_\infty}, \tag{2.1}$$

where ω is the turbine rotor angular velocity.

2.3. *Planar particle image velocimetry*

In this study, planar PIV has been employed to measure the velocity in the turbine wake on a stream-parallel vertical plane; the out-of-plane velocity component is not measured
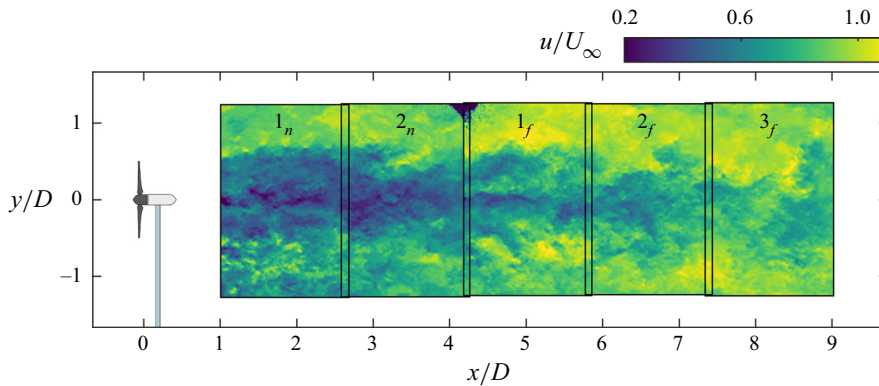
963 A19-6

Figure 1. Planar PIV set-up with the cameras fields of view in the near-wake (1_n and 2_n) and in the far-wake (1_f, 2_f and 3_f), including an instantaneous estimate of the streamwise velocity in the turbine wake. All dimensions to scale.

by this technique. The nomenclature that is used in the remainder of the paper defines x to be the streamwise coordinate, positive in the direction of the flow, and y to be the stream-normal, vertical coordinate, positive upwards; both are dimensional and are adimensionalised by the turbine diameter D. The origin of this reference frame is placed at the centre of the turbine rotor, so that x defines the streamwise distance from the rotor-swept plane, and y measures the distance from the turbine axis of rotation. The convention used here employs the label u for the streamwise component and v for the vertical component of velocity; both are made adimensional by the free stream speed U_∞. Moreover, Reynolds decomposition is used to separate the velocity into a time-averaged and a fluctuating, zero-mean component:

$$u(t) = \overline{u(t)} + u'(t) = U + u'(t), \tag{2.2}$$

where the overline denotes time-averaging, a capital letter represents a quantity constant in time and the prime symbol denotes a signal having zero time-mean.

Figure 1 reports a schematic representation of the planar PIV set-up used during this study. Three Imager Pro LX cameras were used to obtain the five fields of view reported in figure 1, which were illuminated by a Litron Bernoulli PIV laser: initially, two cameras simultaneously acquired the velocity field for streamwise distances of 1–4.2 rotor diameters downstream of the turbine; these are indicated as positions 1_n and 2_n in the figure. Subsequently, these cameras were moved, and a third camera was added to acquire between 4.1 and 9 diameters of downstream distance; these are locations 1_f to 3_f. All cameras fields of view have dimensions of 300 mm in the x-direction and 450 mm in the y-direction in object-plane units, or 1.67×2.5 rotor diameters; all fields of view overlap the previous and next by a strip 15 mm wide and 450 mm tall, which allows for the statistics fields to be stitched together along the whole span of the measurement domain. Moreover, instantaneous velocity fields are stitched between cameras 1_n and 2_n, as these were acquired simultaneously, and between cameras 1_f to 3_f for the same reason. Processing of the PIV particle displacement snapshots was carried out with LaVision DaVis, specifying an initial window size of 96×96 px and a final window size of 48×48 px with a 75 % overlap between adjacent windows: this results in an overall vector spacing of 1 velocity vector per 1.1 mm in both the x- and y-directions, or 162 vectors in one rotor diameter. Due to the large magnification factor that had to be employed to image the fields of view, tracking particles had a size of approximately 1 px in image-plane

963 A19-7

units, which lead to the phenomenon of peak-locking as described by Christensen (2004). To alleviate the effect of this on the computed statistics, the histogram normalisation correction algorithm presented by Hearst & Ganapathisubramani (2015) was applied to all correlation maps in image-plane units of displacement, prior to the application of a calibration to convert these into object-plane units of velocity. The velocity fields were acquired at a frequency of $0.6\,\mathrm{Hz}$: for a free stream speed of $8\,\mathrm{m\,s^{-1}}$, this corresponds to a displacement in the free stream of 74 diameters of the wind turbine, equal to the length of the wind tunnel test section; for this reason, the velocity realisations are assumed to be statistically independent. Velocity snapshots were phase-locked to the instantaneous position of the turbine rotor, to ensure a uniform distribution of all phases in the computed statistics; this was realised by timing the laser discharge to the index signal of a rotary encoder installed on the turbine shaft. A total of six phases were recorded, at a distance of $0°$, $20°$, $40°$, $60°$, $80°$ and $100°$ from the reference rotor position; as the turbine rotor has three blades, the resulting velocity field is understood to be periodic to a $120°$ rotation of the turbine rotor. A total of 300 instantaneous snapshots of velocity were acquired for each phase: unless otherwise mentioned, statistics were computed on the full dataset consisting of 1800 snapshots per test case. Uncertainty in the instantaneous velocity measurements was estimated by DaVis to be equal to $1.5\,\%$ of the measured values in the near-wake fields of view and $1.0\,\%$ in the far-wake fields, with these values being constant between test cases. This was estimated following the method presented by Wieneke (2015).

2.4. *Test cases*

The turbine wake was generated under 18 different conditions: these were parametrised with the operating tip-speed ratio of the turbine and the free stream turbulence conditions to which the turbine was subject. The turbine was operated at three distinct values of tip-speed ratio λ: these were $\lambda = 1.9$, for which the turbine generates low power and thrust, and the flow around the blades is mostly stalled; $\lambda = 3.8$, for which the turbine generates the most power; and $\lambda = 4.7$, at which the thrust generated is at its maximum. Curves of power and thrust generated by the turbine have previously been reported by Gambuzza & Ganapathisubramani (2021) as adimensional power and thrust coefficients (respectively C_P and C_T): these are defined as

$$C_P = \frac{Q\,\omega}{\frac{1}{2}\rho U_\infty^{\,3}\pi r_{tip}^2}, \tag{2.3}$$

$$C_T = \frac{T}{\frac{1}{2}\rho U_\infty^{\,2}\pi r_{tip}^2}, \tag{2.4}$$

where Q is the torque generated by the rotor, ω is its angular velocity, and the product of these quantities is the mechanical power harvested by the turbine, T is the turbine thrust and ρ is the air density. The values of C_T generated by the turbine for the different λ at which it was operated are listed in table 2: as reported by Gambuzza & Ganapathisubramani (2021), little effect of the free stream turbulence characteristics is seen on these values.

The active grid has been used to generate six different free stream turbulence conditions: in this work, these are classified based on their turbulence intensity

$$I_\infty = \frac{\sqrt{\overline{u'^2}}}{U_\infty}, \tag{2.5}$$

963 A19-8

λ	C_T
1.9	0.52
3.8	0.76
4.7	0.80

Table 2. Turbine thrust coefficient C_T as a function of the tip-speed ratio λ for the operating conditions presented in this study.

Name	L	M1	M2	H1	H2	H3
U_∞ (m s^{-1})	8.0	8.0	8.0	8.0	8.0	8.0
I_∞ (%)	3.0	7.5	8.8	11.5	11.3	11.6
T_0	0.1	0.9	1.0	1.0	6.3	10.5
Ro	—	2	5	2	40	60
Wings	—	P	P	F	P	P

Table 3. Free stream turbulence characteristics of the generated inflow conditions, and active grid operating parameters (F, full wings; P, pierced wings).

and their integral time scale T_0, computed as

$$T_0 = \int_0^{\tau_0} \rho_{uu}(\tau)\,\mathrm{d}\tau, \tag{2.6}$$

where $\rho_{uu}(\tau)$ is the autocorrelation coefficient of $u'(t)$ and τ_0 is the first value of τ for which $\rho_{uu}(\tau) = 0$. This last quantity is presented in the remainder of the paper as normalised by the convective time scale D/U_∞. To compute both I_∞ and T_0, hot-wire anemometry was used to measure the free stream velocity in an otherwise empty test section, on a 5×2 grid at the centre of the test section spanning the rotor-swept area: more details on the hot-wire anemometry setup is included in Gambuzza & Ganapathisubramani (2021). The characteristics of the six flows generated are summarised in table 3: these are named L for the low-turbulence test case, M1 and M2 for the medium I_∞, and H1 to H3 for the high turbulence intensity test cases.

The free stream turbulence spectra are presented in figure 2: in this, the flows are divided in two families, one exhibiting the canonical distribution of energy in the spectrum of Kolmogorov (1941), which are reported in figure 2(*a,c*) and are characterised by $T_0 \leq 1$, and a second for which free stream turbulence intensity I_∞ is approximately constant, but the distribution of this does not follow that of the Kolmogorov spectrum, showing a marked spectral gap for adimensional frequencies around 1×10^{-1} and a narrowband contribution at low frequencies. This can be, for instance, thought to be analogous to the meso-scale peak observed in the spectrum of the atmospheric boundary layer (der Hoven 1957; Smedman-Högström & Högström 1975), although the ratio between the frequency of this peak and the start of the inertial subrange is approximately one order of magnitude, instead of the three-to-four orders seen in the literature. Flows H2 and H3 are thus labelled non-Kolmogorov-like flows in the remainder of the text. This is a desired feature, as previous studies of wind turbine wakes in turbulence employ turbulence whose spectra are Kolmogorov-like (Chamorro & Porté-Agel 2009; Barlas, Buckingham & van Beeck 2016; Deskos *et al.* 2020; Neunaber *et al.* 2021). As it was discussed in § 1, this is often an assumption that is not challenged in the literature, namely that the distribution of power
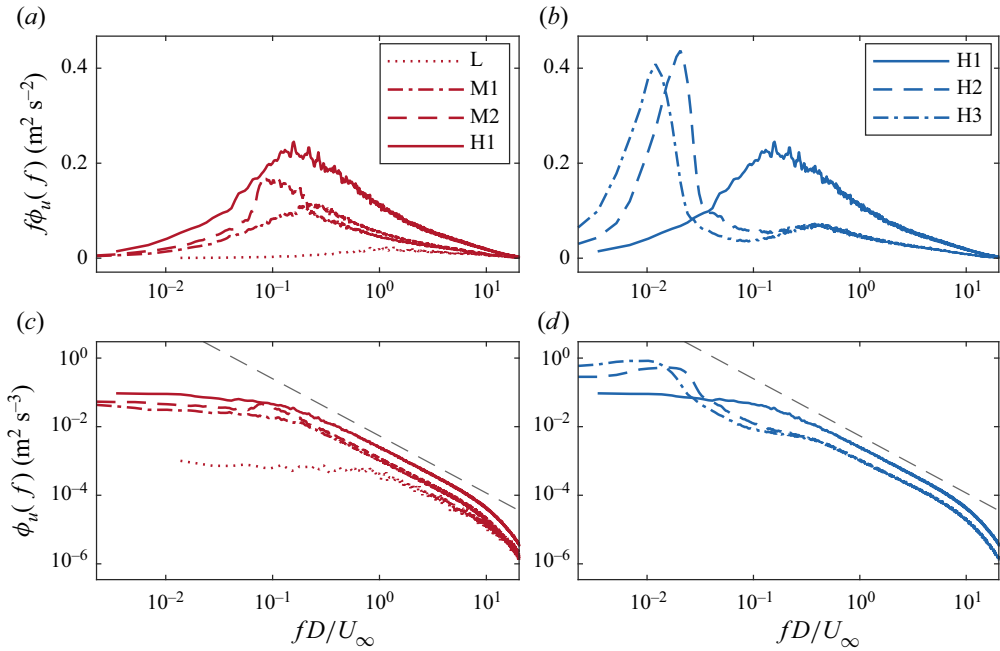
Figure 2. (*a*,*b*) Spectra of the streamwise component of free stream turbulence $\phi_u(f)$ premultiplied by the frequency axis versus adimensional frequency for flows at integral time scale $T_0 \leq 1$ (Kolmogorov-like flows, *a*) and flows at equivalent turbulence intensity I_∞ (non-Kolmogorov flows, *b*). (*c*,*d*) Same spectra plotted as non-premultiplied on canonical log-log axes along with $-5/3$ slope (dashed grey).

in the incoming turbulence spectrum does not affect the development of a wind turbine wake. Note that, while flows H2 and H3 exhibit a large value of T_0, it would be incorrect to assume those are the result of very-large-scale structures: assuming Taylor's hypothesis to hold true, an estimate for the large-eddy size can be given by

$$L_0 = T_0 D, \tag{2.7}$$

which, for flow H3, results in an approximate value of 1.8 m, or twice the test-section width and three times the test section height. It must therefore be accepted that, for flows H2 and H3 presented here, Taylor's hypothesis need not hold as the high integral time scale of these flows is instead representative of a low-frequency change in the bulk free stream velocity as seen by the turbine. In practical terms, these non-Kolmogorov-like flows are generating by actuating the motion of the active grid agitator wings at lower speeds than those used for Kolmogorov-like flows: this can be quantified introducing the grid Rossby number Ro, defined as

$$Ro = \frac{U_\infty}{\Omega M}, \tag{2.8}$$

where Ω is the mean angular velocity of the active grid rods. For the two non-Kolmogorov-like test cases, the slow rotation of the rods translates into a slow change of the blockage generated by the grid, which in turn induces slow changes in the bulk free stream speed. This can be easily appreciated from the time series of velocity reported in figure 3.
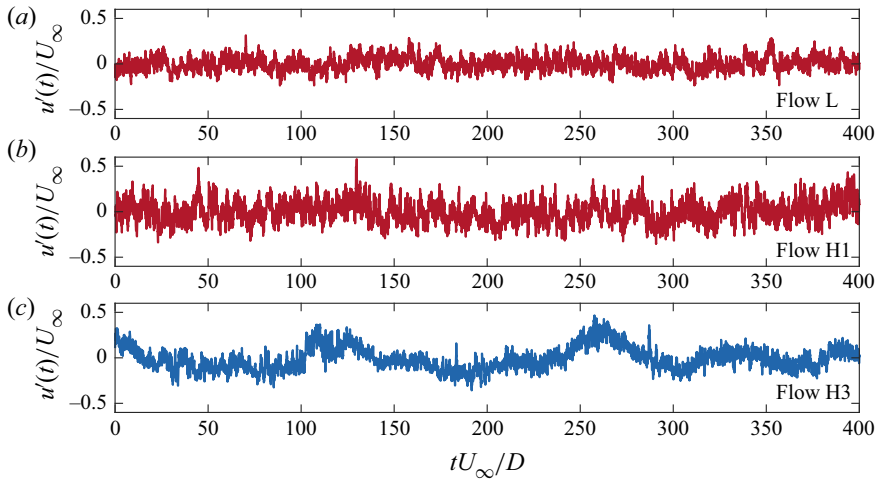
963 A19-10

Figure 3. Time series of free stream velocity $u(t)$ for three selected test cases, plotted versus time normalised by the convective time scale D/U_∞.

3. Results and discussion

As briefly introduced in § 1, one of the most important parameters of the turbine wake is the velocity deficit ΔU. This is defined as a function of the streamwise distance from the turbine as

$$\frac{\Delta U}{U_\infty} = \frac{U_\infty - \min_y(U(x, y))}{U_\infty}, \tag{3.1}$$

where the dependency of U on y is removed by taking the minimum in that direction. This parameter is of interest to a wind farm designer as this sets the streamwise distance between rows of turbines in a wind farm.

Figure 4 reports the trends of the velocity deficit ΔU for all inflow conditions analysed in this study. In particular, figure 4(a) isolates the trends for the Kolmogorov-like flows: it can clearly be seen that an increase in the free stream turbulence intensity generates a monotonic decrease of the velocity deficit, and therefore a faster wake recovery and a shorter overall wake length. This is often connected to an increase in the turbulent mixing, favouring the homogenisation of velocity between the low-speed wake and the higher-momentum free stream surrounding it (Medici & Alfredsson 2006; Chamorro & Porté-Agel 2009), a behaviour that is also seen for other bluff bodies in turbulence (Hearst, Gomit & Ganapathisubramani 2016). Figure 4(b) instead collects the family of flows at equivalent I_∞ and, even in this case, important differences between the wake velocity profiles are seen. In particular, the wakes generated for the non-Kolmogorov-like flows H2 and H3 are seen to be only slightly different, and these appear to evolve more slowly both with respect to the equivalent-I_∞ flow H1, and more surprisingly to flow M1, which has a much smaller value of free stream turbulence intensity. In fact, only the wake generated under flow L, which here has been taken as the reference for a low-turbulence flow, evolves more slowly.

Data reported in the previous figure 4 were obtained by fixing the turbine tip-speed ratio and, ultimately, its thrust. However, figure 5 reports the value of $\Delta U/U_\infty$ for all flows to which the turbine has been subjected and for all three values of C_T here studied; free stream turbulence intensity is reported on the horizontal axis and free stream integral
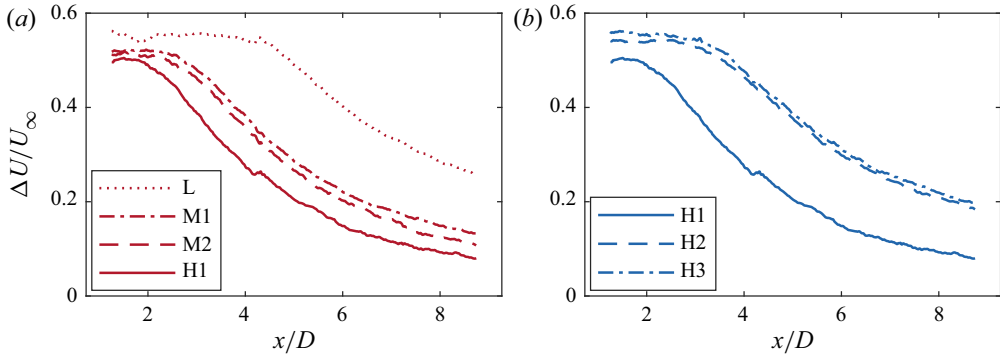
Figure 4. Maximum velocity deficit $\Delta U/U_\infty$ as a function of the streamwise distance from the turbine x/D for (*a*) the Kolmogorov-like flows at $T_0 \leq 1$ and (*b*) for the equivalent I_∞ flows. Turbine operating at peak power-generating $\lambda = 3.8$.
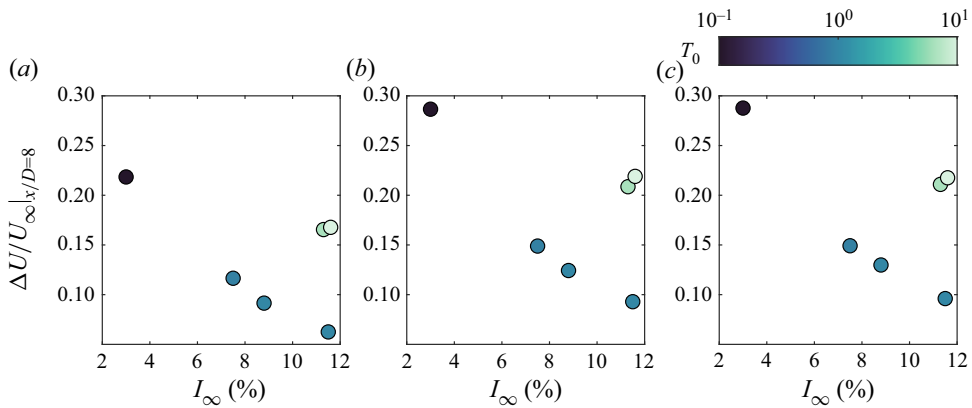

Figure 5. Velocity deficit $\Delta U/U_\infty$ at $x/D = 8$ for all operating conditions, as a function of the free stream turbulence intensity I_∞ (horizontal axis) and integral time scale T_0 (colour, note the logarithmic axis), for the turbine operating at (*a*) $\lambda = 1.9$, (*b*) $\lambda = 3.8$ and (*c*) $\lambda = 4.7$.

time scale is reported as the colour of the markers. The results of figure 4 can clearly be generalised to all values of C_T here studied and, thus, these are representative of a peculiar behaviour of the wind turbine. The trend of velocity deficit with turbulence intensity, limiting the analysis to the Kolmogorov-like flows of $T_0 \leq 1$, is clearly decreasing; as no data have been acquired for values of $I_\infty > 12\%$, it cannot be said whether this tends asymptotically to zero or not. This is an important distinction: an asymptotic trend to zero would suggest that the turbine wake can be arbitrarily shortened by a large enough value of free stream turbulence. However, a trend to a small but finite value would instead hint to a behaviour for which the mean flow in the wake is unaffected by an increase of I_∞ after a certain threshold, a behaviour that is similar to what is observed for boundary layers generated in free stream turbulence (Sharp, Neuscamman & Warhaft 2009; Dogan, Hanson & Ganapathisubramani 2016).

Wakes of turbines are also seen to meander, that is, change their instantaneous trajectory. This is a phenomenon that is understood to be driven primarily by instabilities in the shear layer (Heisel *et al.* 2018); in the field, instantaneous changes in wind direction also contribute to this motion, a behaviour that is not simulated here. To identify the
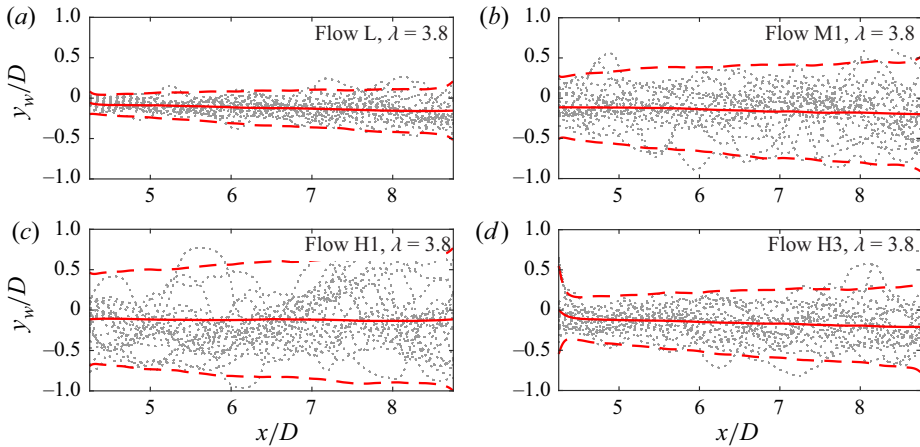
963 A19-12

Figure 6. Instantaneous trajectory of the wake $y_w(x)$ (dotted grey lines, 20 random trajectories shown per test case), alongside mean wake trajectory (solid red line) and boundaries of the wake meandering region (dashed red lines). Data shown for (*a*) inflow L, (*b*) M1, (*c*) H1 and (*d*) H3; turbine operating at $\lambda = 3.8$ for all four panels.

instantaneous trajectories of the wake from the individual velocity snapshots, the method of Howard *et al.* (2015) is used: in this, the instantaneous wake trajectory is determined for each x as

$$y_w(x, t) = \underset{y}{\mathrm{argmin}}(u(x, y, t)), \tag{3.2}$$

which is then low-pass filtered to remove all contributions having a wavelength smaller than $D/2$. Figure 6 reports, for each of the edge cases at $\lambda = 3.8$, 20 randomly chosen instantaneous trajectories in dotted grey. Alongside these, the mean wake trajectory is found by averaging the instantaneous y_w in time, and the extent of the meandering region is reported as twice the standard deviation of the instantaneous wake trajectories. Figure 7 reports instead the standard deviation of y_w in time for any given value of x/D. Assuming that the distribution of y_w for a given x/D is Gaussian, the point of minimum velocity in the wake is within the bounds

$$\left[\frac{\overline{y_w}}{D} - 2\frac{\sqrt{\overline{y_w'^2}}}{D}; \frac{\overline{y_w}}{D} + 2\frac{\sqrt{\overline{y_w'^2}}}{D}\right] \tag{3.3}$$

in 95 % of all observations and, therefore, this value is representative of the extent of the wake meandering motion in space. It can be appreciated that the width of this region increases both with distance from the turbine, a phenomenon observed for the wakes of solid and porous disks by España *et al.* (2011) and in LES of wind farms by Foti *et al.* (2019), and with the free stream turbulence intensity content I_∞. Once again, by limiting the analysis to the Kolmogorov-like flows and the extent of the wake meandering region (see data reported in figure 7*a*), it is easy to appreciate that the extent of the wake meandering increases with the free stream turbulence content; that is, the wake meandering amplitude increases with increasing I_∞. However, the largest increase happens between flows L and M1, in conjunction with the increase in integral time scale of the flow T_0, suggesting that this is mostly due to the size of the eddies introduced in the free stream; adding more turbulence without affecting its scales increases the extent of meandering
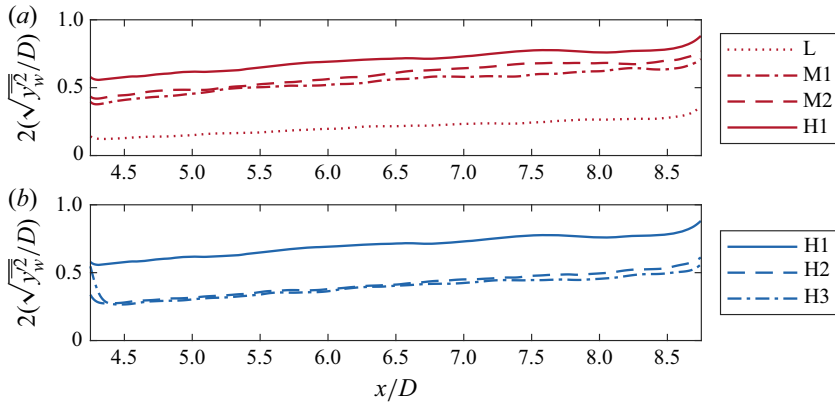
Figure 7. Extent of the meandering region estimated as twice the standard deviation of the instantaneous wake trajectories for (*a*) the Kolmogorov-like flows at $T_0 \leq 1$ and (*b*) the flows at equivalent I_∞. Turbine operating at $\lambda = 3.8$.
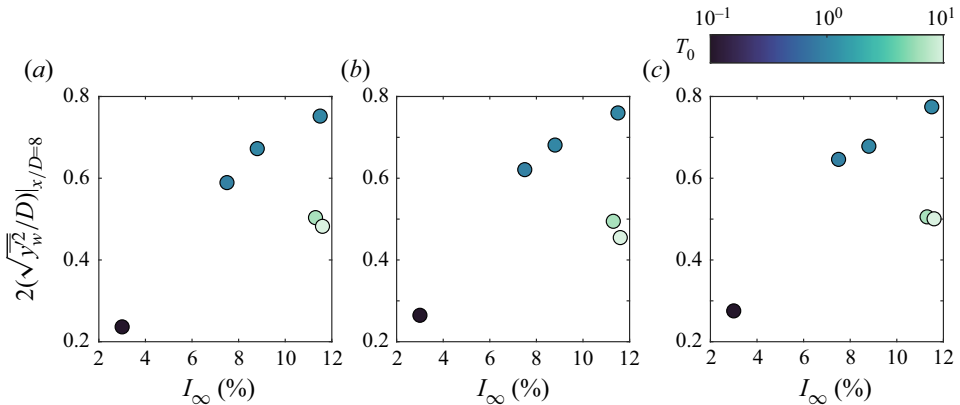

Figure 8. Extent of the meandering region at $x/D = 8$ as a function of the inflow conditions, for (*a*) $\lambda = 1.9$, (*b*) $\lambda = 3.8$ and (*c*) $\lambda = 4.7$.

by inducing shear layer instabilities (Medici & Alfredsson 2006), although its effects are of smaller intensity when compared to those of mean-flow convection. However, the non-Kolmogorov flows H2 and H3 are seen to result in little wake meandering whose extent is, like for the velocity deficit, lower than that generated by flow M1 but higher than that of the low-turbulence flow L. This is despite a large value of T_0 that should suggest eddies 5 to 10 times larger between these flows and the equivalent-I_∞ flow H1; however, one must remember the remark given in § 2.4, for which Taylor's frozen hypothesis need not hold for the high-T_0 flows and the large value of T_0 is not necessarily representative of the large scale structure size. This can readily be seen by extracting the value of the wake meandering amplitude at $x/D = 8$, which is shown in figure 8: the largest increase in the wake meandering amplitude is observed going from $I_\infty = 3\%$ to $I_\infty = 7.5\%$. While the wakes generated by the two non-Kolmogorov flows are characterised by meandering, their amplitude is only intermediate between those of flow L ($I_\infty = 3\%$) and flow H1 ($I_\infty = 11.5\%$), and lower than those of flows at intermediate I_∞, a finding that holds true at all values of tip-speed ratio here investigated.
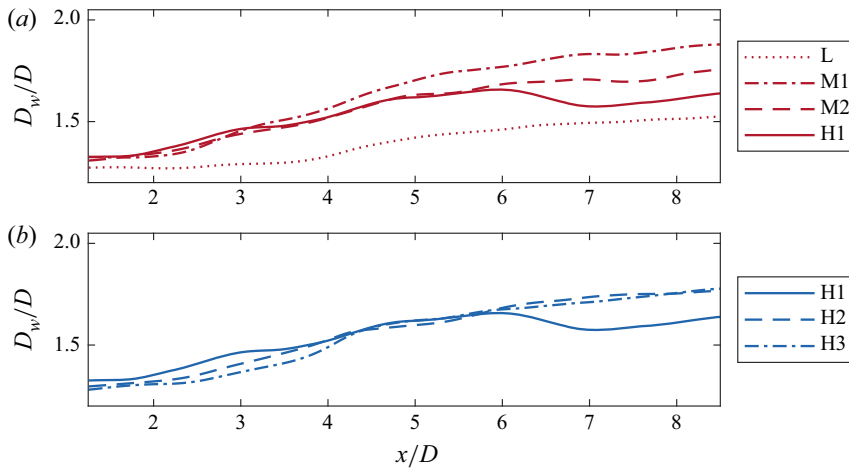
963 A19-14

Figure 9. Adimensional wake diameter D_w/D measured at $\lambda = 3.8$, for (*a*) inflows with $T_0 \leq 1$ and (*b*) flows at equivalent I_∞.

In addition to the velocity deficit, the wake diameter is an important parameter as this sets the lateral spacing between turbines in a farm; its growth in the streamwise direction is often taken as representative of the wake recovery rate and thus of the extent of the wake in the streamwise direction (Jensen 1983; Frandsen *et al.* 2006). Figure 9 reports the wake diameter D_w measured for all investigated inflows with the turbine operating at $\lambda = 3.8$; as the presence of the mast affects the flow for $y/D < 0$, this is computed as twice the distance between the iso-line of $U = U_\infty$ and the mean wake trajectory $\overline{y_w}$, which itself is obtained by averaging the instantaneous wake trajectories shown in the previous figure 6. To highlight the large-scale trends, the trends of D_w are also low-pass filtered to remove contributions with wavelengths below $D/2$. The most immediate result that can be observed is that, for the investigated cases at $\lambda = 3.8$, little effect of the inflow is seen on the initial evolution of the wake and in particular of its slope: all flows except flow L result in wakes with similar diameters for $x/D < 4$. This is an important observation, as this means that inferring the wake recovery rate k from the wake diameter trend might lead to inaccurate estimations in the field. For the high-turbulence flow H1, one can even observe that the trend of D_w is not linear for all values of x/D, and instead plateaus after $x/D = 7$; while it could be argued that this is due to the presence of the wind tunnel walls, this does not seem to affect the evolution of all other wakes developed under different inflows, meaning the reason for this constant wake diameter might be found in the turbulence enveloping the wake. Following the approach of Pope (2000), one can observe that the momentum deficit flows is an invariant of the wake equal to the turbine thrust. The streamwise momentum equation can be written as

$$T = \rho \left(\int_{A_i} U_\infty^2 \, \mathrm{d}A - \int_{A_w} U^2 \, \mathrm{d}A \right), \tag{3.4}$$

where T is the turbine thrust, ρ is the fluid density, and A_i and A_w are two sections of a stream tube containing the wind turbine far upstream and downstream of the turbine, respectively. As T is constant, so must be the product $U^2 \, \mathrm{d}A$ on A_w; however, it can be seen from the data presented in figures 4(*a*) and 9(*a*) that for $x/D > 7$, D_w and therefore A_w are constant while U changes. It is at this point important to note that (3.4) only holds for A_w sufficiently downstream of the turbine, so that the mean momentum
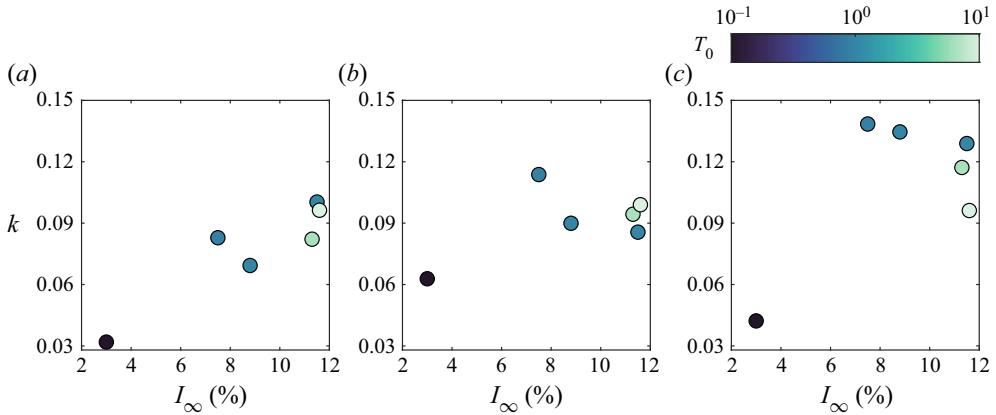
Figure 10. Wake growth rate k found as the slope of the linear regression of D_w/D; data for (*a*) $\lambda = 1.9$, (*b*) $\lambda = 3.8$ and (*c*) $\lambda = 4.7$. Data from panel (*b*) were already presented in figure 9.

convection $U(\partial U/\partial x)$ dominates over the turbulent transport in both the streamwise and stream-normal directions $\partial \overline{u'^2}/\partial x$ and $\partial \overline{u'v'}/\partial y$, respectively. Data reported in § 3.3 will show that the case of flow H1 and $\lambda = 3.8$ is also the test case for which the terms of the Reynolds stress tensor are the largest; this, coupled with the fact that at $x/D \geq 7$, $U \simeq U_\infty$, driving $U(\partial U/\partial x)$ to low values, makes the assumptions under which (3.4) does not necessarily hold.

The value of k can be obtained, as a function of the free stream turbulence characteristics, as the slope of the linear regression of D_w/D; to account for the plateau in D_w for the test case of flow H1 and $\lambda = 3.8$, the linear regression is performed for $x/D < 5$ for all test cases except for flow L. In the case of this flow, the regression is instead performed for $4 < x/D < 6$ to account for the initial plateau in D_w. Data reported in figure 10 show that the trend of k is erratic with both turbulence intensity and integral time scale: for the low thrust case of $\lambda = 1.9$ (figure 10*a*), a somewhat linear trend of k with I_∞ is seen, with a small effect of T_0 on the wake expansion; this last observation is similarly seen for $\lambda = 3.8$, for which however the trend of k with I_∞ is not linear, and the wake that experiences the largest expansion is that developed under the moderate turbulence of flow M1.

The data presented in this section therefore show how the wake generated by the isolated turbine is affected by both the free stream turbulence intensity I_∞ and its frequency content, which in this study has been parametrised as its integral time scale T_0. However, the approach followed in this section has not attempted to quantify these effects, nor has it explained the physical phenomena that drive this evolution or these trends. The next section will therefore present a parametrisation of the wake generated by the wind turbine based on frequently used analytical wake models, which will then be leveraged in the next sections to quantify the effects of turbulence on the wake developed by the turbine.

3.1. *Quantifying the effects of turbulence*

As mentioned in § 1, analytical wake models are powerful tools that are often used both in literature and in the field to represent the complex turbine wake in a simplified fashion. These operate by assuming the existence of a relationship between the velocity in any point of the wake and a reduced set of parameters: for instance, the widespread Gaussian wake
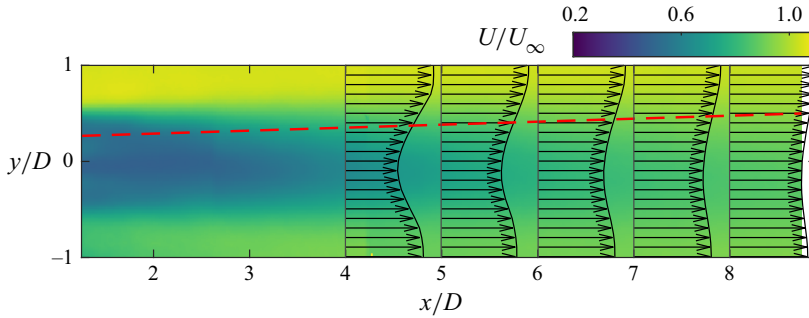
963 A19-16

Figure 11. Determination of k^* from PIV measurements in the mean wake. In colour, mean streamwise velocity component; in black arrows, selected velocity profiles; in dashed red, linear regression of $\sigma_w(x)$. Data for flow M1, $\lambda = 3.8$.

model, developed by Bastankhah & Porté-Agel ([2014](#)), assumes that the velocity in any point of the wake is described by the set of equations

$$\frac{\Delta U}{U_\infty} = \left(1 - \sqrt{1 - \frac{C_T}{8(\sigma_w/D)^2}}\right) \exp\left(-\frac{(r/D)^2}{2(\sigma_w/D)^2}\right), \tag{3.5}$$

$$\frac{\sigma_w}{D} = k^* \frac{x}{D} + \epsilon, \tag{3.6}$$

where r is the radial coordinate away from the turbine axis and k^* is a parameter that serves the role of the wake expansion rate k in the previous section. Regarding the definition of ϵ, the authors show that from considerations on the total mass flow deficit rate across the turbine disk, one must have

$$\epsilon = 0.25\sqrt{\beta}, \tag{3.7}$$

where

$$\beta = \frac{1}{2}\frac{1 + \sqrt{1 - C_T}}{\sqrt{1 - C_T}}. \tag{3.8}$$

However, the authors show that the Gaussian model provides estimates that better match the LES data of turbines in the atmospheric boundary layer by assuming that $\epsilon = 0.2\sqrt{\beta}$. One must note that, as the authors explain, the difference between these formulations consists in the distance necessary for the wake to equalise its pressure with the surrounding free stream: in particular, $\epsilon = 0.25\sqrt{\beta}$ assumes that this is verified on the turbine disc, while $\epsilon = 0.2\sqrt{\beta}$ assumes a non-zero distance is necessary to attain this.

As full knowledge of the wake geometry is known from the PIV velocity fields, one can compute the value of k^* for each operating condition and inflow as outlined in figure 11: for every value of x/D, a velocity profile is obtained and fitted to a Gaussian profile, with the standard deviation of the fitted profile being an estimate of $\sigma_w(x)$. The value of k^* is then the slope of the linear regression of this last quantity. As for the previous data on the wake diameter D_w presented in figure 9, the fitting is limited to the range $0 < y/D < 1$ as the presence of the mast has impacted the symmetry of the wake; moreover, as the velocity profiles need not be Gaussian close to the turbine, especially at low values of I_∞ (Medici & Alfredsson [2006](#)), σ_w is only computed for $x/D \geq 4$.

Figure 12(a) reports, for all wakes obtained at $\lambda = 3.8$ and thus constant $C_T = 0.76$, the trends of velocity deficit previously reported in figure 4 where the values on the
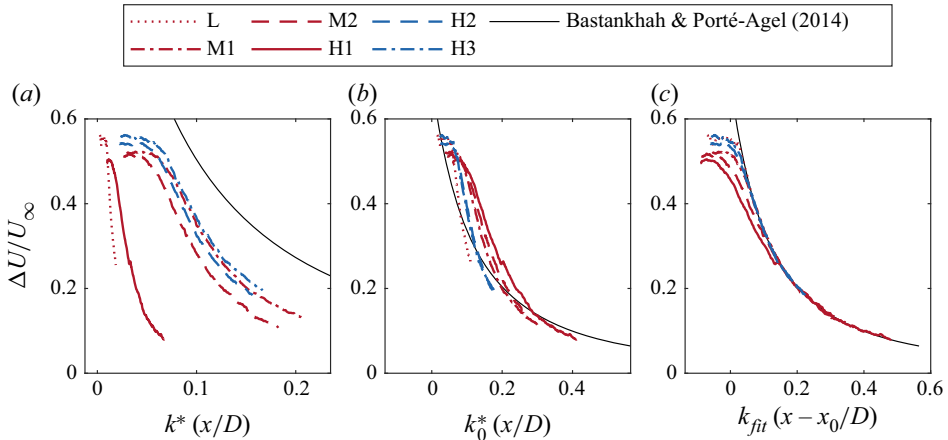
Figure 12. Comparison of the wake velocity deficit trends $\Delta U/U_\infty$ with the trend predicted by Bastankhah & Porté-Agel (2014), (a) assuming $\epsilon_0 = 0.2\sqrt{\beta}$ and k^* inferred from wake profile fitting, (b) assuming $\epsilon_0 = 0.2\sqrt{\beta}$ and best-fitting k_0^*, and (c) with the trends obtained by determining the best-fit values of k^* and x_0 assuming $\epsilon_0 = 0.25\sqrt{\beta}$. Data for $\lambda = 3.8$.

horizontal axis are the distance from the turbine multiplied by the k^* attained in each specific operating condition: it can be appreciated that none of the curves collapse on the prediction offered by Bastankhah & Porté-Agel (2014). Figure 12(b) instead presents the velocity deficit trends where the distance from the turbine is normalised by k_0^*: this parameter is determined so that the velocity trends reported minimise, in a least-square sense, the difference with the expected trend from the Gaussian model, as it is standard in approaching this problem in industrial settings. Instead, figure 12(c) reports the same trends as in figure 12(a) having normalised the distance from the wind turbine by using two parameters: a virtual origin x_0 and an alternative value of k^*, which has been labelled k_{fit}. The formulation of (3.6) used in the remainder of this paper is therefore

$$\frac{\sigma_w}{D} = k_{fit}\frac{x - x_0}{D} + 0.25\sqrt{\beta}. \tag{3.9}$$

Both the virtual origin x_0 and the alternative wake recovery rate k_{fit} have been obtained as the two parameters that minimise the sum of squared residuals between each measured trend of ΔU and the predicted curve according to (3.5), having imposed $r/D = 0$. The use of a virtual origin to describe the evolution of bluff-body wakes in turbulence is a widely employed method for other bluff bodies such as porous disks (Rind & Castro 2012a,b; Pal & Sarkar 2015), spheres (Spedding, Browand & Fincham 1996) or even when describing wakes of bodies in turbulent boundary layers (Sakamoto & Arie 1983); this approach has been recently shown to be valid for wakes generated by utility-scale turbines in the atmospheric boundary layer (Neunaber *et al.* 2022). While the physical meaning of the wake recovery rate is immediate, the plotted trends in figure 12(c) highlight how the virtual origin x_0 is loosely connected to the extent of the interval of x for which the velocity deficit is constant. In this case, it can be seen that a collapse, especially for large values of x/D, is obtained regardless of the inflow conditions, improving both on the assumption that k^* can be inferred from the wake diameter growth rate, and on the current industry standard of finding the best-fit k^* and employing no virtual origin. While this shows that the Gaussian wake model can be tuned to predict the wakes of turbines in a wide array of
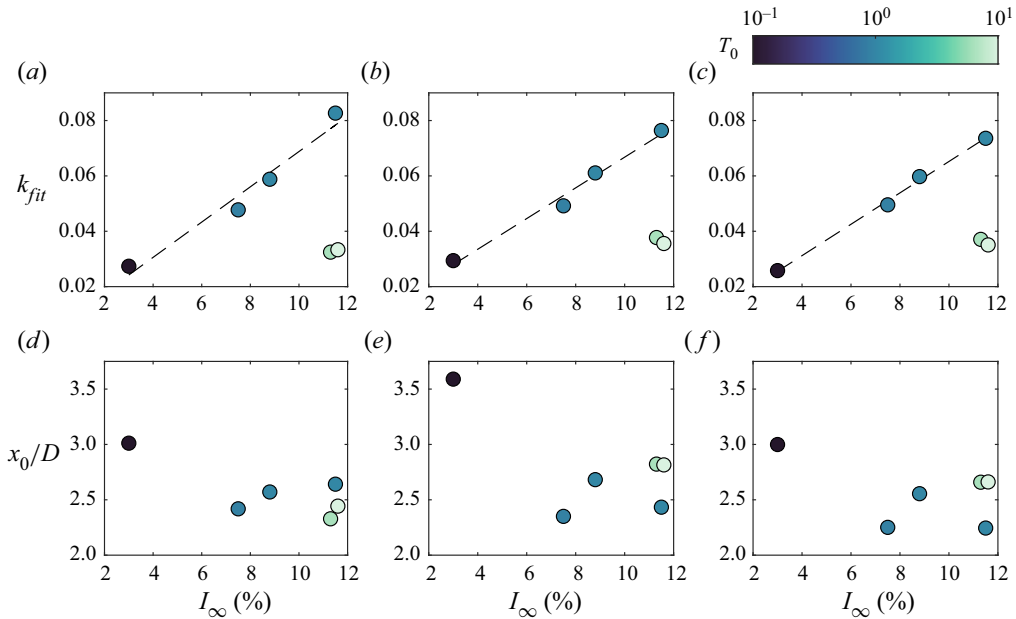
963 A19-18

Figure 13. Trends of (*a–c*) k_{fit} and (*d–f*) x_0/D with the free stream turbulence properties I_∞ (horizontal axis) and T_0 (colour axis). Data for (*a,d*) $\lambda = 1.9$, (*b,e*) $\lambda = 3.8$ and (*c,f*) $\lambda = 4.7$.

both realistic and non-Kolmogorov-like flows, this also quantifies the effect of turbulence on the wake generated by a wind turbine.

Figure 13 reports the values of the two parameters used, k_{fit} and x_0, for all test cases investigated in this study. For all the turbine operating points, it can be seen that k_{fit} assumes a linear trend with I_∞ if one limits the analysis to the Kolmogorov-like flows. This is in good agreement with previous literature, namely the work of Niayifar & Porté-Agel (2016) and that of Peña *et al.* (2016) on the Jensen wake model (Jensen 1983), where the authors show how the linear relationship between the wake recovery rate and I_∞ can be recovered assuming the vertical velocity profile is well described by the Monin–Obukhov similarity theory (Monin & Obukhov 1954); one must however note that no vertical velocity profile is present in our measurements, and thus the linear relationship between k_{fit} and I_∞ holds even outside the atmospheric boundary layer. The general trend of k_{fit} mimics well what is already seen on the wake velocity deficit, for instance in figures 4 and 5, where wakes exhibiting higher values of ΔU far from the turbine have low values of k_{fit} and vice versa.

Instead, the virtual origin x_0 is seen to be less affected by the free stream turbulence conditions: generally, this value is the highest for the low-turbulence case of flow L, regardless of the turbine thrust coefficient, and all other flows exhibit a value of $x_0/D \simeq$ 2.5, only moderately affected by C_T and free stream turbulence. It is also interesting to note that, limiting our attention to high-turbulence flows, the value of x_0 is higher for the non-Kolmogorov flows for the two test cases at high C_T than it is for the Kolmogorov-like flow H1, while this trend appears reversed for the low-C_T test case of $\lambda = 1.9$. However, one must note that the scatter between the values of x_0 obtained for flows H1, H2 and H3 is comparable to the scatter between those of all flows of $T_0 = 1$. It is therefore possible that, while the inclusion of the virtual origin x_0 helps in fitting the curves with

the Gaussian wake model, the value of this parameter need not vary with inflow conditions beyond a certain threshold of I_∞.

The parametrisation of the wake in its recovery rate k_{fit} and its virtual origin x_0 also provides a convenient separation between two regions in the wake: in the next section, we will argue that the extent of the near-wake is loosely related to the trends of x_0 and to the stability of the helical vortex set enveloping the wake. Conversely, one can interpret the value of k_{fit} to be the main parameter that drives the wake evolution for large distances downstream of the turbine, and thus to be representative of the far-wake evolution.

3.2. *Influence on near-wake extent*

Customarily, the wake of a wind turbine is often divided in two regions: a near-wake, where the rotor geometry affects the local velocity field, and a far-wake which is instead independent of the turbine geometry and self-similarity is attained (De Cillis *et al.* 2020); however, seldom a quantitative definition of their extent is given. A number of methods have been presented in the literature to estimate the location of the transition between one region and the other, based on considerations of the turbulent kinetic energy content (Wu & Porté-Agel 2012; Sørensen *et al.* 2015; De Cillis *et al.* 2020) or on the onset of wake meandering (Howard *et al.* 2015). It can be understood that these methods only provide a qualitative estimation of this transition, as there is no hard boundary between the near- and the far-wake. This however does not mean there is no merit in estimating the near-wake length, as trends of these estimations can still provide valuable information as comparison between test cases. In this work, the definition of near-wake length is slightly changed from the one presented by Wu & Porté-Agel (2012): having defined the turbulent kinetic energy as

$$\kappa = \tfrac{1}{2}\left(\overline{u'^2} + \overline{v'^2} + \overline{w'^2}\right), \tag{3.10}$$

its mean advection is

$$\boldsymbol{U} \cdot \nabla\kappa = U\frac{\partial \kappa}{\partial x} + V\frac{\partial \kappa}{\partial y} + W\frac{\partial \kappa}{\partial z}, \tag{3.11}$$

where $\boldsymbol{U} = (U; V; W)$ is the time-averaged velocity vector. Note that for steady flows, this is equal to the material derivative of κ:

$$\frac{\mathrm{D}\kappa}{\mathrm{D}t} = \frac{\partial \kappa}{\partial t} + \boldsymbol{U} \cdot \nabla\kappa = \boldsymbol{U} \cdot \nabla\kappa, \tag{3.12}$$

as $\partial/\partial t = 0$ in steady-state conditions. The near-wake is then defined as the location where $\mathrm{D}\kappa/\mathrm{D}t > 0$ and vice versa for the far-wake. Physically, the interpretations are as follows: as a flow parcel traverses the rotor-swept plane, its turbulent kinetic energy increases under the effect of both the circulation generated by the blades and the vorticity these shed, either as a vortex sheet or as the system of tip- and root-vortices. As the parcel travels downstream, it will cede this to its surrounding; therefore, a positive value of this material derivative denotes that the evolution of the particle is driven by its interaction with the turbine and vice versa.

As the data collected consist of the two in-plane components of velocity u and v, it is impossible to compute the full turbulent kinetic energy as defined in (3.10) as no information is available on w'; similarly, without W, the term relative to the advection of κ in the z-direction cannot be computed. For this reason, the definitions in (3.11) and
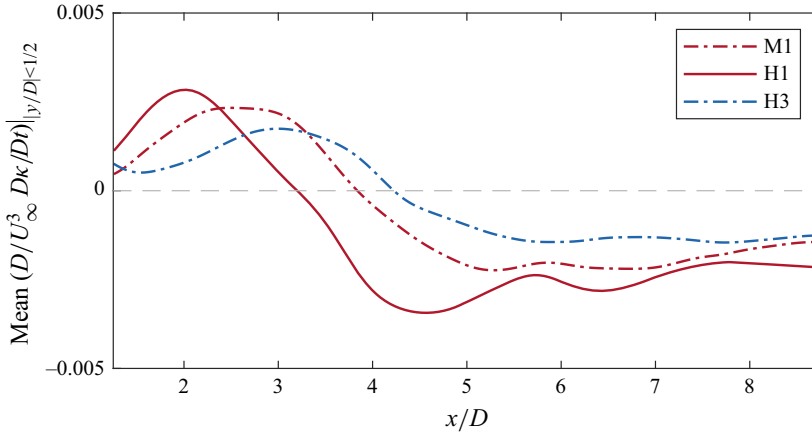
963 A19-20

Figure 14. Trends of mean material derivative of turbulent kinetic energy $D\kappa/Dt$ for $|y/D| < \frac{1}{2}$ as a function of the streamwise distance from the turbine for inflows M1, H1 and H3. Turbine operating at $\lambda = 3.8$.

(3.10) have been implemented by assuming that $v/w = O(1)$ and $\partial/\partial y \simeq \partial/\partial z$; thus, the turbulent kinetic energy is estimated as

$$\kappa = \tfrac{1}{2}\left(\overline{u'^2} + 2\overline{v'^2}\right), \tag{3.13}$$

and its material derivative is estimated as

$$\frac{D\kappa}{Dt} = U\frac{\partial\kappa}{\partial x} + 2V\frac{\partial\kappa}{\partial y}, \tag{3.14}$$

which is an assumption that holds true particularly close to the wake centre, as the wake is somewhat axisymmetric, and gets progressively less so farther from that, as an azimuthal velocity component is introduced as a result of the torque generated by the blades and the assumption that $v \simeq w$ need not hold (Medici & Alfredsson 2006).

Figure 14 reports the trends of the material derivative of κ with distance from the turbine; this is adimensionalised by the term D/U_∞^3. To reduce the effect of experimental noise on the measurements, the trends reported have been obtained by averaging the value of κ for $|y/D| < 1/2$, equivalent to limiting this analysis only to particles that have traversed the turbine rotor. Moreover, each trend is low-pass filtered to remove all components having a wavelength smaller than $D/2$. The trends highlight a clear distinction between the two regions at positive and negative $D\kappa/Dt$, as well as showing that this value does not trend to a zero value at long distances from the turbine. This is expected and is due to the natural decay of turbulence with free stream distance, proper of both grid-generated turbulence (Kistler & Vrebalovich 1966; Hearst & Lavoie 2016) and bluff-body wakes (Wygnanski, Champagne & Marasli 1986). Defining the value of x at which $D\kappa/Dt$ changes sign as x_κ, one can observe the trends of this parameter with free stream turbulence characteristics in figure 15. Data for $\lambda = 1.7$ are not reported as $D\kappa/Dt$ is negative along the whole domain and no change in sign is observed; for this operating condition, the torque generated by the blades is marginally lower than that at $\lambda = 4.7$ and considerably lower than that at $\lambda = 3.8$ (Gambuzza & Ganapathisubramani 2021): the circulation generated by the blades is therefore lower and so is the intensity of the tip- and root-vortices generated by the blades. This, paired with a lower λ and therefore more spaced vortices, might have led to a less intense interaction between the turbine and the flow traversing the rotor-swept plane.
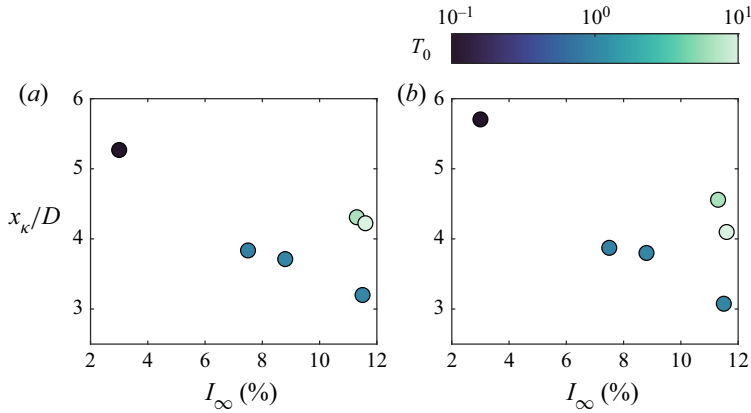
Figure 15. Location of the change of sign x_κ/D in the spatial mean of $D\kappa/Dt$ as a function of the free stream turbulence intensity I_∞ (horizontal axis) and integral time scale T_0 (colour axis), shown for (*a*) $\lambda = 3.8$ and (*b*) $\lambda = 4.7$.

The trends of x_κ are somewhat similar to those of the virtual origin x_0 reported in figure 13(*e,f*) for the two high-λ test cases: in particular, it can in both cases be seen that the low-I_∞ inflow conditions result simultaneously in a high x_0 and a high x_κ. Moreover, among the three flows at $I_\infty \approx 11.5\%$, the Kolmogorov-like conditions of flow H1 are the ones that result in the lowest values of both x_0 and x_κ. However, focusing one's attention only to the Kolmogorov-like flows at $T_0 \leq 1$, x_κ shows a clear decreasing trend that is not readily seen in the values of the virtual origin. This suggests that the changes in value of the virtual origin are broadly affected by the same mechanisms that regulate the near-to-far-wake transition, although x_0 cannot be taken as representative of the transition distance.

To understand the conditions that drive the evolution of the near-wake, it is useful to observe the behaviour of the tip-vortices shed by the turbine. Vortex identification from an instantaneous velocity snapshot can be carried out with a number of techniques; in this work, the Q-criterion (Hunt, Wray & Moin 1988; Jeong & Hussain 1995; Haller 2005) has been employed due to the simplicity of the underlying equations and the ease of adaptation to planar data. For an instantaneous velocity field $\boldsymbol{u}(t) = (u(t), v(t))$, the in-plane value of Q is computed as

$$Q = -\frac{1}{2}\left(\left(\frac{\partial u}{\partial x}\right)^2 + 2\frac{\partial u}{\partial y}\frac{\partial v}{\partial x} + \left(\frac{\partial v}{\partial y}\right)^2\right), \tag{3.15}$$

and vortices are individuated as continuous regions in the flow where $Q > 0$. Figure 16 reports the map of Q for a representative velocity snapshot obtained for the operating conditions of $\lambda = 3.8$ and inflow L, along with the methodology used to individuate the location and intensity of individual vortices. Given a computed map of Q, contiguous regions of positive Q are individuated as the regions bounded by iso-lines of Q equal to a certain threshold, which in this case has been chosen as $0.3(D/U_\infty)^2$; the iso-lines are then approximated with the best-fitting ellipse, with the centre of the ellipse being used as the location of the vortex and the value of Q at the centre being an indication of the vortex intensity.

The position of the vortices is shown in figure 17 for four edge-cases, all having the turbine operating at $\lambda = 3.8$. From these, it can be seen how the low turbulence intensity of flow L results in a very coherent and stable train of vortices mostly concentrated around
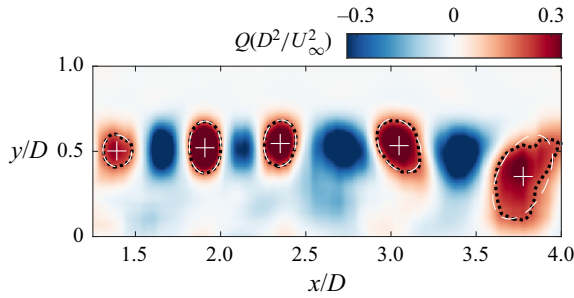
963 A19-22

Figure 16. Identification of the tip-vortices location (white plus signs) from isocontours of Q-criterion (black dotted) approximated with best-fitting ellipses (white dashed). Data displayed are those of a representative snapshot obtained at $\lambda = 3.8$ and inflow L.
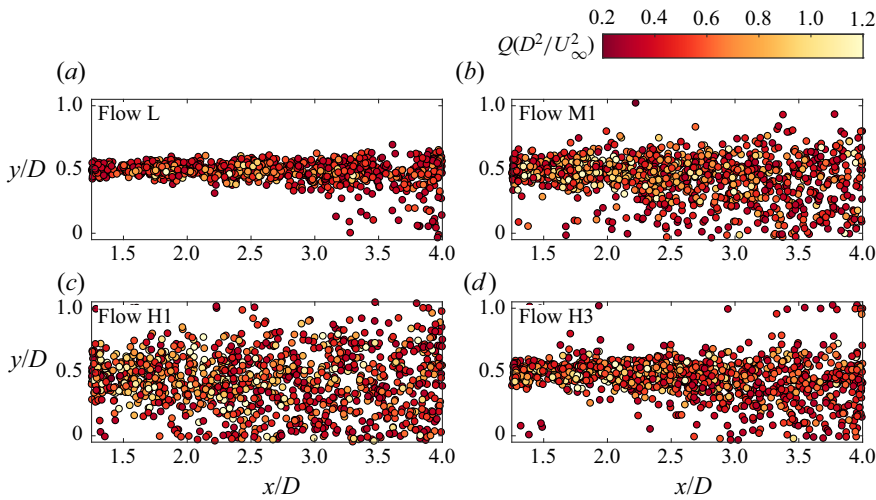

Figure 17. Instantaneous position of the tip-vortices for inflows (*a*) L, (*b*) M1, (*c*) H1 and (*d*) H3, coloured by their peak Q. Turbine operating at $\lambda = 3.8$. For clarity, a random subset of 1200 individual vortices is shown for every panel.

the tip-height line at $y/D = 0.5$, with some small instability setting on at $x/D > 3.5$. For the two Kolmogorov-like inflows at high I_∞, namely M1 and H1, shear layer instability is favoured by the high amount of free stream turbulence and the vortices positions are more erratic: this shear layer instability in turn drives the wake meandering seen in figure 6 for the same two test cases. The test case of the non-Kolmogorov flow H3 is instead seen, despite the same value of I_∞, to result in an initially more stable shear layer, with the tip-vortices occupying a region close to $y/D = 0.5$, larger than that generated under inflow L but visibly bounded, unlike that of the two previous flows M1 and H1; this initial shear layer stability is possibly connected to the less intense wake meandering observed in figure 6. The mechanisms that drive the breakdown of the tip-vortex set are well known and extensively studied in the literature. Ivanell *et al.* (2010), Sarmast *et al.* (2014) and Lignarolo *et al.* (2015) show how, at a certain distance from the turbine, the phenomenon of leapfrogging, that is, the interaction between a vortex and the preceding or following one, contributes to the breakdown of this structure; in particular, Ivanell *et al.* (2010) shows that the additional perturbations due, for instance, to free stream

turbulence favour the onset of leapfrogging closer to the rotor, which is further confirmed by Sarmast *et al.* (2014). In the case of the results reported in figure 17, the leapfrogging cannot be directly observed; however, it can be reasonably assumed that the more erratic trajectory of these vortices in the case of inflows M1 and H1 does indeed favour interaction between adjacent vortices closer to the rotor.

It has been previously reported in the literature that the presence of the helical vortex set envelopes the wake and prevents transfer of momentum between the wake and the surrounding free stream, thus delaying the wake evolution (Lignarolo *et al.* 2014, 2015; De Cillis *et al.* 2020): this suggests that the initial wake evolution is hampered by the presence of a stable shear layer and thus by a train of coherent vortices, which effectively shield the near-wake from the free stream. This can be easily visualised, for the test cases here reported, with quadrant analysis to characterise the events on the mean vortices trajectory. At these locations, a $v' < 0$ denotes flow crossing the vortices trajectory from the high-momentum free stream to the wake and $v' > 0$ denotes conversely motion from the wake outwards; simultaneously, $u' > 0$ indicates motion of high-momentum flow and $u' < 0$ indicates that of low-momentum flow. Wake evolution is therefore promoted either by the sweep of high-momentum flow inside the wake, for which $u' > 0$ and $v' < 0$, or by ejection of low-momentum flow from the wake, for which $u' < 0$ and $v' > 0$; vice versa, wake evolution is hampered by interaction events, for which u' and v' have the same sign. Thus, the individual contributions to the in-plane Reynolds shear stress $\overline{u'v'}$ in each quadrant can be defined as

$$\overline{u'v'}_j = \int_{Q_j} u'v' \, P(u', v') \, \mathrm{d}u' \, \mathrm{d}v', \tag{3.16}$$

where Q_j denotes the jth quadrant and $P(u', v')$ is the joint probability density function for an event in the (u', v')-space. Moreover, one can define

$$\overline{u'v'}_{1+3} = \overline{u'v'}_1 + \overline{u'v'}_3 \tag{3.17}$$

and likewise for $\overline{u'v'}_{2+4}$.

The trends of the quadrant contributions on the mean vortices trajectory are reported in figure 18, divided into events that hamper the wake evolution (figure 18*a*) and those that favour it (figure 18*b*). By observing the trends of the second and fourth quadrant, for which a negative value indicates more intense sweep and ejection events and therefore a faster-evolving wake, one can see that the fast-evolving wake under flow H1 is indeed the one that results in the largest value of $\overline{u'v'}_{2+4}$ and thus in the most intense interaction between free stream and wake. For the Kolmogorov-like flows, the intensity of these events is roughly proportional to the free stream turbulence intensity I_∞; this relationship however does not hold for the non-Kolmogorov test case of inflow H3, which is seen instead to have a value of Q2 and Q4 events slightly lower than those of flow M1, despite the larger I_∞. By instead observing the trends of Q1 and Q3 events, it can be seen that the relationship between events intensity and I_∞ need not necessarily hold close to the wind turbine: in fact, for small values of x/D, flow L results in interaction events that are more intense than those developed for inflow M1 and H, despite the much less intense inflow turbulence; this however decays rapidly and by $x/D = 2$, flow L is once again the one for which the events intensity is the smallest. It is instead more interesting to observe the intensity of interaction events for flow H3, which are seen to be more intense than those of flow M1 along the whole of the near-wake, and larger than those of flow H1 close to the turbine until $x/D \approx 2.25$.
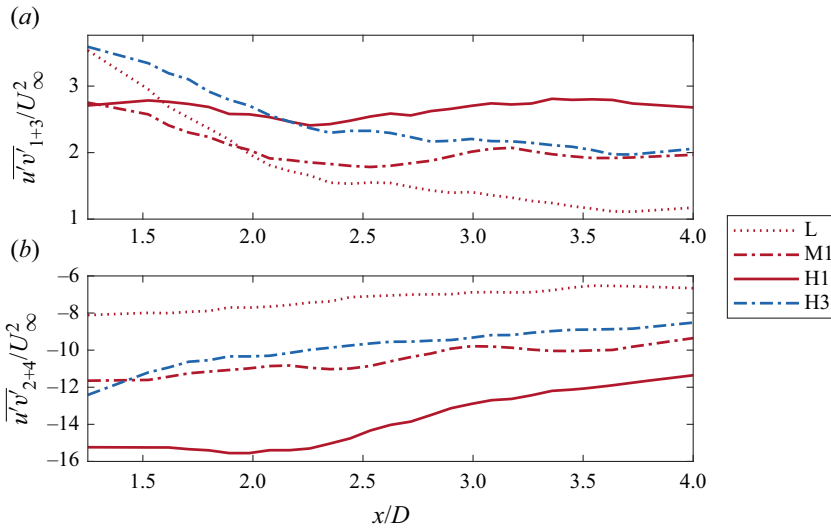
963 A19-24

Figure 18. Sum of the contributions to the Reynolds shear stress in (*a*) the first and third quadrant and in (*b*) the second and fourth quadrant, on the mean tip-vortices trajectory. Data for inflows L, M1, H1 and H3, and $\lambda = 3.8$.

From the data here presented, it is evident that the main cause of the delayed onset of wake evolution has to be found in the robustness of the train of tip-vortices, which is in turn driven by the shear layer instability. A stable shear layer inhibits sweep and ejection events, and favours interaction events. The effect of free stream turbulence intensity I_∞ on the shear layer stability is non-trivial, as it has been seen that a non-Kolmogorov-like inflow with energy content skewed towards low-frequency contributions results in a more stable shear layer than a Kolmogorov-like flow.

3.3. *Far-wake evolution*

While the stability of the enveloping helical vortex structure is consistent with the near-to-far-wake transition, this phenomenon does not provide an explanation for the rate at which the wake recovers, and thus for the different values of the wake recovery rate k_{fit} as seen in figure 13. To understand the drivers of wake evolution in the far-wake region, it can be useful to approach the Reynolds-averaged Navier–Stokes equations, in particular, the one that describes the evolution of the streamwise momentum component: for a steady three-dimensional flow, this can be expressed as

$$U\frac{\partial U}{\partial x} + V\frac{\partial U}{\partial y} + W\frac{\partial U}{\partial z} + \frac{\partial \overline{u'^2}}{\partial x} + \frac{\partial \overline{u'v'}}{\partial y} + \frac{\partial \overline{u'w'}}{\partial z} = -\frac{1}{\rho}\frac{\partial P}{\partial x}, \tag{3.18}$$

where the contributions due to viscosity have been neglected as the Reynolds number is high. The momentum equation in the *y*-direction can be simplified (Townsend 1999) to the expression

$$\frac{\partial \overline{v'^2}}{\partial y} + \frac{\partial \overline{v'w'}}{\partial z} = -\frac{1}{\rho}\frac{\partial P}{\partial y}. \tag{3.19}$$

As for the turbulent kinetic energy computation in § 3.2, one can remedy the lack of information on the out-of-plane components of velocity by assuming that $\partial/\partial y \simeq \partial/\partial z$

963 A19-25

and $\overline{v'^2} \simeq \overline{w'^2}$. While this is a strong assumption, it can be thought as reasonable especially close to the wake centreline: the wake generated by the wind turbine being roughly axisymmetric, both y and z represent radial directions from the wake axis outwards. With these assumptions, (3.18) near the wake centreline can be expressed in the simplified form:

$$U\frac{\partial U}{\partial x} = -2V\frac{\partial U}{\partial y} - \frac{\partial(\overline{u'^2} - 2\overline{v'^2})}{\partial x} - 2\frac{\partial \overline{u'v'}}{\partial y} + R, \tag{3.20}$$

where R is a residual term that takes into account the differences between the left- and right-hand sides of the equation due to the simplifying assumptions employed in this formulation, and the $-2\overline{v'^2}$ in the second term of the right-hand side derives from (3.19): with the simplifying assumption employed, one has

$$2\frac{\partial \overline{v'^2}}{\partial y} = -\frac{1}{\rho}\frac{\partial P}{\partial y} \Rightarrow -\frac{1}{\rho}\frac{\partial P}{\partial x} = 2\frac{\partial \overline{v'^2}}{\partial x} + \frac{1}{\rho}\frac{\partial P_0}{\partial x}, \tag{3.21}$$

with the terms at the right-hand side of the implication sign being obtained by integrating the left-hand side in y and then taking the derivative in x. In particular, P_0 is the integration coefficient that stems from the integration of $\partial P/\partial y$ in y and thus is constant in the vertical direction: for this reason, its evolution in x is due to the presence of a potential pressure gradient due to the facility, which is arbitrarily assumed to be negligible here to simplify the analysis. The variation of the terms of (3.20) in x/D is reported, for four test cases having $\lambda = 3.8$, in figure 19, along with the value of the virtual origin computed for each wake. It can be seen that for the cases of high I_∞ (inflows M1, H1 and H3), the dominant term of those at the right-hand side of (3.20) is indeed the one relative to the in-plane Reynolds shear stress, as it is often assumed for far-wakes (Tennekes & Lumley 1972), and that for $x/D > x_0/D$, the residual R is often small enough to be negligible; this is however not true for the case of the low I_∞ of flow L, for which instead there is a non-negligible contribution of the mean advection term $V\partial U/\partial y$. This is consistent with results previously published in the literature, where higher Reynolds shear stresses generated in the turbine wake result in a swifter evolution of the streamwise velocity component (Chamorro & Porté-Agel 2010), or base flows exhibiting a larger Reynolds shear stress upstream of the wind turbine result in a faster wake evolution despite similar values of free stream I_∞ (Zhang, Markfort & Porté-Agel 2013).

Assuming therefore that, at least for the high-I_∞ flows,

$$U\frac{\partial U}{\partial x} \simeq -2\frac{\partial \overline{u'v'}}{\partial y} \tag{3.22}$$

holds true for $x/D > x_0/D$ and on the wake centreline, one can obtain an analytical relationship between the value of the wake recovery rate k^* and the in-plane Reynolds shear stress at the centreline. In fact, noting that

$$U\frac{\partial U}{\partial x} = \frac{1}{2}\frac{\partial U^2}{\partial x}, \tag{3.23}$$

one can integrate (3.22) to yield

$$\int_{x_0}^{x_{fw}} \frac{\partial U^2}{\partial x}\,\mathrm{d}x = U_{fw}^2 - U_{x_0}^2 = -4\int_{x_0}^{x_{fw}} \frac{\partial \overline{u'v'}}{\partial y}\,\mathrm{d}x, \tag{3.24}$$

where x_{fw} is a far-downstream station, U_{x_0} is the value of U at the virtual origin and likewise U_{fw} is the value of U downstream of the turbine. The modified formulation of
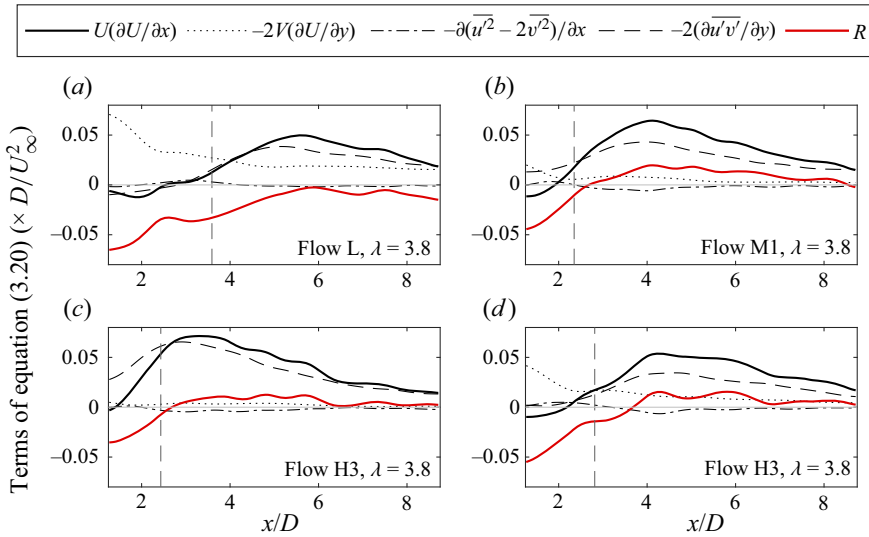
963 A19-26

Figure 19. Terms of (3.20), made adimensional by multiplication with D/U_∞^2, for the inflows (*a*) L, (*b*) M1, (*c*) H1 and (*d*) H3, (black and red lines), along with the value of x_0 (dashed vertical line); turbine operating at $\lambda = 3.8$.

Bastankhah & Porté-Agel ([2014](#)) presented in this paper can be used to estimate the values of U in the wake: arbitrarily choosing $x_{fw} = x_0 + nD$, one has

$$\frac{U_{fw}^2}{U_\infty{}^2} = 1 - \frac{C_T}{8(\epsilon_0 + nk^*)^2}, \tag{3.25}$$

$$\frac{U_{x_0}^2}{U_\infty{}^2} = 1 - \frac{C_T}{8\,\epsilon_0^2}, \tag{3.26}$$

which, substituted in (3.24), yield

$$\frac{C_T}{8\,\epsilon_0^2} - \frac{C_T}{8(\epsilon_0 + nk^*)^2} = -4\int_{x_0}^{x_0+nD} \frac{1}{U_\infty{}^2}\frac{\partial\overline{u'v'}}{\partial y}\,\mathrm{d}x. \tag{3.27}$$

This is a quadratic equation in k^*: its positive solution is found as

$$k_{est}^* = \frac{\epsilon_0}{n}\left(\sqrt{\frac{C_T}{C_T + 32\,I_{RSS}\,\epsilon_0^2}} - 1\right), \tag{3.28}$$

where I_{RSS} refers to the integral of the Reynolds shear stress derivatives at the right-hand side of (3.27):

$$I_{RSS} = \int_{x_0}^{x_0+nD} \frac{1}{U_\infty{}^2}\frac{\partial\overline{u'v'}}{\partial y}\,\mathrm{d}x. \tag{3.29}$$

Figure 20 reports the values of the derivative of the in-plane Reynolds shear stress on the wake centreline, here approximated as the horizontal axis having $y/D = 0$. It can be seen that this quantity is, for the Kolmogorov-like flows, increasing with increasing I_∞. This relationship however does not hold for the non-Kolmogorov-like test case of flow H3, for which the derivative of the Reynolds shear stress is the lowest of all test cases
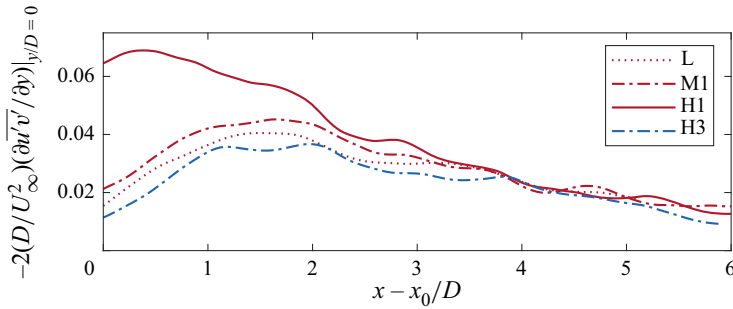
Figure 20. Distribution of the derivative of Reynolds shear stress on the wake centreline from the location of the virtual origin onwards. Data for $\lambda = 3.8$.
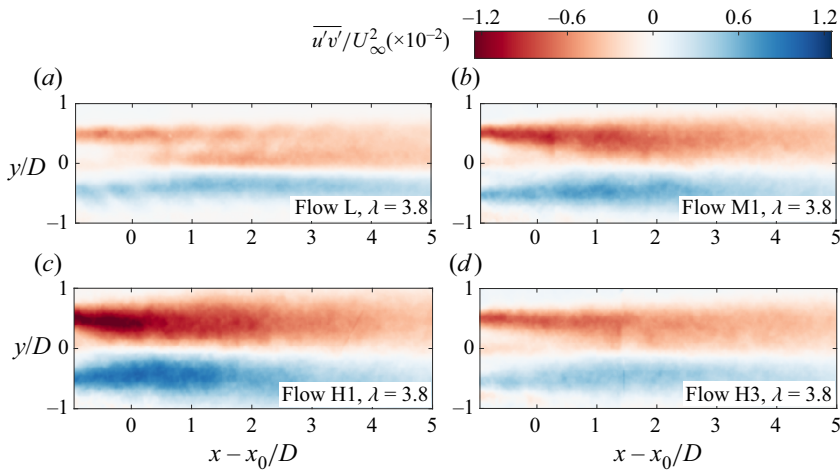

Figure 21. Fields of Reynolds shear stress $\overline{u'v'}$ in the turbine wake for the test cases presented in figure 20.

here analysed. Figure 21 reports the fields of the Reynolds shear stress in the turbine wake for the test cases corresponding to the test cases presented in figure 20: from these, it can be appreciated that the effect of the free stream conditions on the quantity plotted in figure 20 are indeed representative of a more general and less localised phenomenon. Indeed, it can be appreciated that flow H1 is the test case for which the Reynolds shear stress is the strongest for low values of x, and that the stress in the wake generated by the test cases M1 and H3 are comparable in absolute values. Moreover, one can notice how, for all test cases, the value of this derivative is similar once a large enough distance from the turbine has been covered, such as for $(x - x_0)/D > 4$, while all differences in these trends are concentrated at small distances from the turbine. This is in accordance with (3.22) and the data reported previously in figure 12, which shows that all streamwise velocity deficit trends tend to the same overall shape (and therefore, the same spatial gradient in the streamwise direction) sufficiently far from the turbine.

The values of k_{fit} obtained from fitting the velocity deficit trends have been reported as square markers in figure 22. Alongside these, we present the values of k_{est}^* obtained by multiplying the result of (3.28) by 4, as this equation appears to underestimate the actual values of k_{fit} by such a factor. Focusing on the medium- and high-λ cases, it can be appreciated that, with the single exception of the low-I_∞ test case at $\lambda = 3.8$, this equation
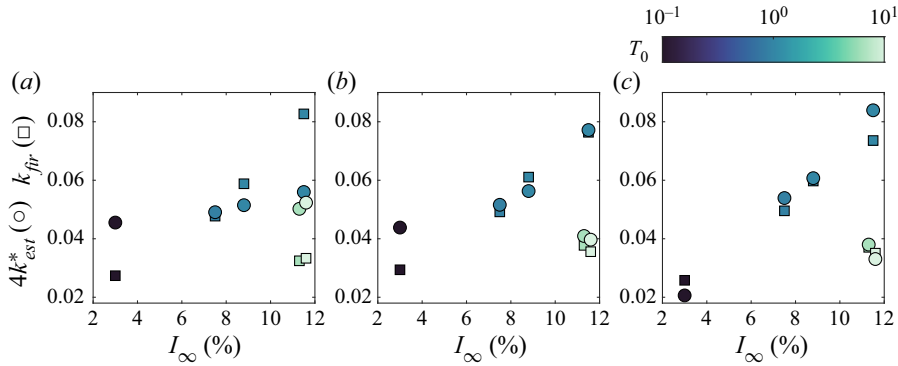
963 A19-28

Figure 22. Estimation of k_{fit} from integration of the Reynolds shear stress on the wake trajectory according to (3.30) (round markers) and comparison with the values found by fitting the wake velocity deficit trends (square markers). Data from (*a*) $\lambda = 1.9$, (*b*) $\lambda = 3.8$ and (*c*) $\lambda = 4.7$.

is able to capture both the linear trend of k^* with I_∞ and the drop in the wake recovery rate for the non-Kolmogorov-like inflow conditions, regardless of the thrust generated by the turbine. However, as it can be seen from figure 22(*a*), this relationship need not hold for the low-C_T case. In this case as well, however, the linear trend of k^* with I_∞ and the drop for high-T_0 flows are recovered. Therefore, it is reasonable to approximate the wake recovery rate k_{fit} as

$$k_{fit} \simeq 4 \frac{\epsilon_0}{n} \left(\sqrt{\frac{C_T}{C_T + 32\, I_{RSS}\, \epsilon_0^2}} - 1 \right) \tag{3.30}$$

for high-thrust operating conditions and high values of I_∞.

Following this, it can be understood that the driver of the mean wake velocity evolution is the Reynolds shear stress: knowing this, it can be expected that flows with higher values of free stream turbulence intensity result in faster-evolving wakes as they favour a larger content of Reynolds shear stress in the wake, which explains the trend of k^* with I_∞, seen to be linear in the literature. A large body of recent literature (Chamorro *et al.* 2015; Tobin *et al.* 2015; Deskos *et al.* 2020; Gambuzza & Ganapathisubramani 2021) has shown a relationship between the spectrum of the incoming velocity fluctuations and the power harvested by a turbine from said incoming velocity field, with the turbine harvesting more power for spectra biased towards lower frequency. It can therefore be assumed that as the turbine harvests power from low-frequency velocity contributions, these will not be present in the wake: in other words, if the turbine acts as a low-pass filter from the point of view of harvested power, it must act as a high-pass filter from the point of view of its wake; this is indeed observed by Tobin & Chamorro (2019), in which the velocity spectra downstream of the turbine are biased towards higher-frequency contributions than those upstream of it. A similar observation is reported by Heisel *et al.* (2018) for data acquired in the wake of a utility-scale wind turbine. The idea that a turbine acts as to remodulate the spectral content in its wake has been also shown from the LES data by Chatterjee & Peet (2018, 2021), where the authors show that for an infinite wind farm, the presence of large scales in the free stream favours the transfer of mean kinetic energy from the free stream to the wake, thus hastening the wake recovery and changing the spectral content of the wake. While this would suggest that flows H2 and H3 should result in a faster-evolving wake, a number of differences are present between these works and the present study.

For instance, in the case of these cited works, the authors present their conclusions in the frame of an infinite turbine; it is possible that, for an isolated turbine, the mechanism of power extraction dominates over that of mean kinetic energy entrainment. Moreover, the length scales of the eddies generated by Chatterjee & Peet (2018) are at most of $O(10D)$, or equivalently corresponding to inflows with high-energy content at $fD/U_\infty = 10^{-1}$. The two high-time scale flows here investigated, namely H2 and H3, instead show peaks in the power spectral distribution at $fD/U_\infty = 10^{-2}$, that is, one order of magnitude lower than what was investigated in the cited works, further suggesting that the mean kinetic energy entrainment mechanics are affected by the free stream content of turbulence in a non-trivial way.

As no time-resolved data are available in the wake of the turbine, the hypothesis that spectra in the wake are biased towards high-frequency contributions cannot be verified; however, one can quantify the dominant scales in the wake by means of two-point correlation. Defining the two-point correlation coefficient between a fixed point (x_f, y_f) and a generic point (x, y) in the domain as

$$R_{uu} = \frac{\overline{u'(x_f, y_f)u'(x, y)}}{\left(\overline{u'^2(x_f, y_f)}\ \overline{u'^2(x, y)}\right)^{1/2}}, \qquad (3.31)$$

the value of R_{uu} acts, in space, as analogous to the classical autocorrelation in time for a time-resolved, single-point measurement. Figure 23 reports the value of R_{uu} for the far-wake generated by the turbine under inflows H1, which is Kolmogorov-like, and H3, which is not; the points that are chosen as fixed are $(x_f/D = 5.5, y_f/D = 0)$ as representative of the flow in the wake, and $(x_f/D = 5.5, y_f/D = 1)$ for the free stream; moreover, the figure also reports the iso-line of $R_{uu} = 0.75$ for all cases. It can be seen that for both the Kolmogorov-like inflow conditions of flow H1 and those of flow H3, the correlation decreases by moving from the free stream to the far-wake: the characteristic lengths of the presented iso-line reduce both in x and y showing a bias towards lower wavelengths in the wake spectral composition, which can be thought of as analogous to the bias towards high-frequency contributions observed by Tobin & Chamorro (2019). Moreover, it can also be observed that while the changes in R_{uu} are limited in the vicinity of the fixed point for the case of flow H1, the difference between the correlation maps for flow H3 is instead more evident: this does further point towards a clear difference between the spectra of the free stream and the wake for non-Kolmogorov flows, as the turbine has harvested the low-frequency, high-wavelength contributions in the free stream.

To quantify this phenomenon, one can attempt to define an equivalent turbulence intensity by purposefully filtering out the low-frequency contributions in the free stream velocity power spectral density:

$$I_{filt}(f_{filt}) = \left(\frac{1}{U_\infty^2} \int_{f_{filt}}^{\infty} \phi_u(f)\, \mathrm{d}f\right)^{1/2}, \qquad (3.32)$$

where f_{filt} is the cut-off frequency of an idealised high-pass filter. Tobin *et al.* (2015) suggests, from comparison between the power spectral densities of the free stream turbulence and the mechanical power generated by the turbine,

$$f_{filt} = \frac{2Q}{J\omega}, \qquad (3.33)$$

where Q is the torque exerted by the turbine on the shaft, J is the rotor moment of inertia and ω is the rotor angular velocity. Additionally, Li, Dong & Yang (2022) suggest that
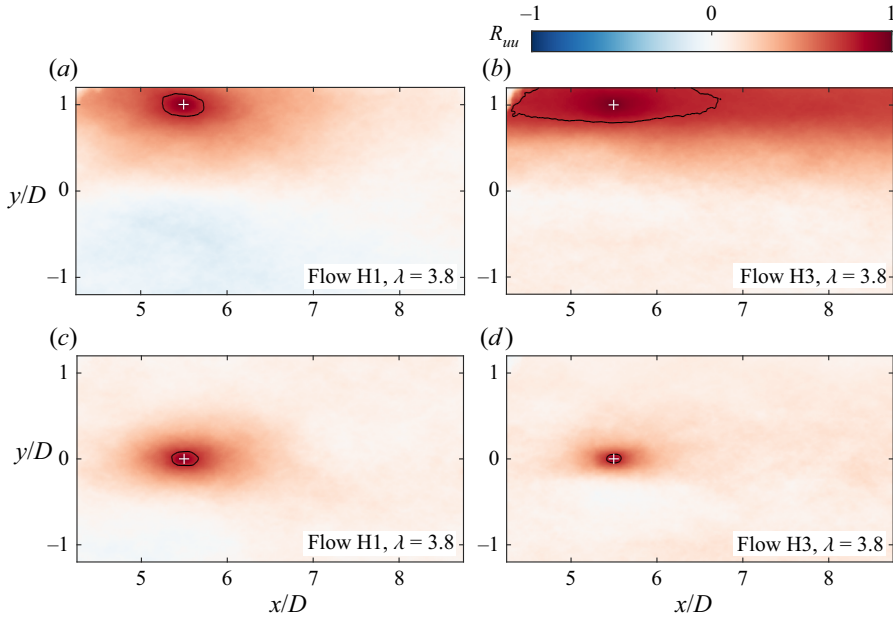
963 A19-30

Figure 23. Two-point correlation coefficient R_{uu} maps in the far-wake of the turbine operating under base flows (*a*,*c*) H1 and (*b*,*d*) H3, and iso-line of $R_{uu} = 0.75$ (black line); fixed point (*a*,*b*) $x_f/D = 5$, $y_f/D = 1$ and (*c*,*d*) $x_f/D = 5$, $y_f/D = 0$ (white plus sign). Turbine operating at $\lambda = 3.8$.

side-to-side motions of a turbine excite wake meandering if these come at a Strouhal number $St = fD/U_\infty$ greater than 0.1; there might thus be merit in using a constant

$$f_{filt} = 0.1 \frac{U_\infty}{D} \tag{3.34}$$

for all test cases. Lastly, if one assumes that the turbine fully converts the low-frequency contributions to the free stream velocity into mechanical power, one could use

$$f_{filt} = \underset{0.05 < St < 20}{\mathrm{argmin}} \ (f\phi_u(f)) \tag{3.35}$$

for the non-Kolmogorov-like flows H2 and H3, and $f_{filt} = 0$ otherwise: this means that $I_{filt} = I_\infty$ for the Kolmogorov-like inflow conditions. Note that, for both flows H2 and H3, (3.35) returns $f_{filt} \approx 0.1(U_\infty/D)$: for this reason, the only difference between the approaches of (3.34) and (3.35) is on whether filtering is applied to the Kolmogorov-like test cases.

Figure 24 shows the values of k_{fit} obtained by fitting the velocity deficit trends of figure 4 as a function of the filtered, equivalent free stream turbulence intensity I_{filt}: the top row employs (3.33), the middle row uses (3.34) and the bottom row uses (3.35) for the non-Kolmogorov-like inflows only, without any filtering of the inflow for the more canonical turbulence cases. The figure shows that, independently of the definition that one employs for f_{filt}, I_{filt} is lower for the non-Kolmogorov-like flows than it is for the more canonical test cases. In particular, using the arbitrary definition of (3.35), one recovers the linear trend of k, this time against I_{filt}, which is the current state-of-the-art in the application of analytical wake models in turbulent inflows (Niayifar & Porté-Agel 2016; Peña *et al.* 2016): this is an additional indicator of a bias towards the remodulation of the wake spectral content by the presence of the turbine, previously seen in the literature.
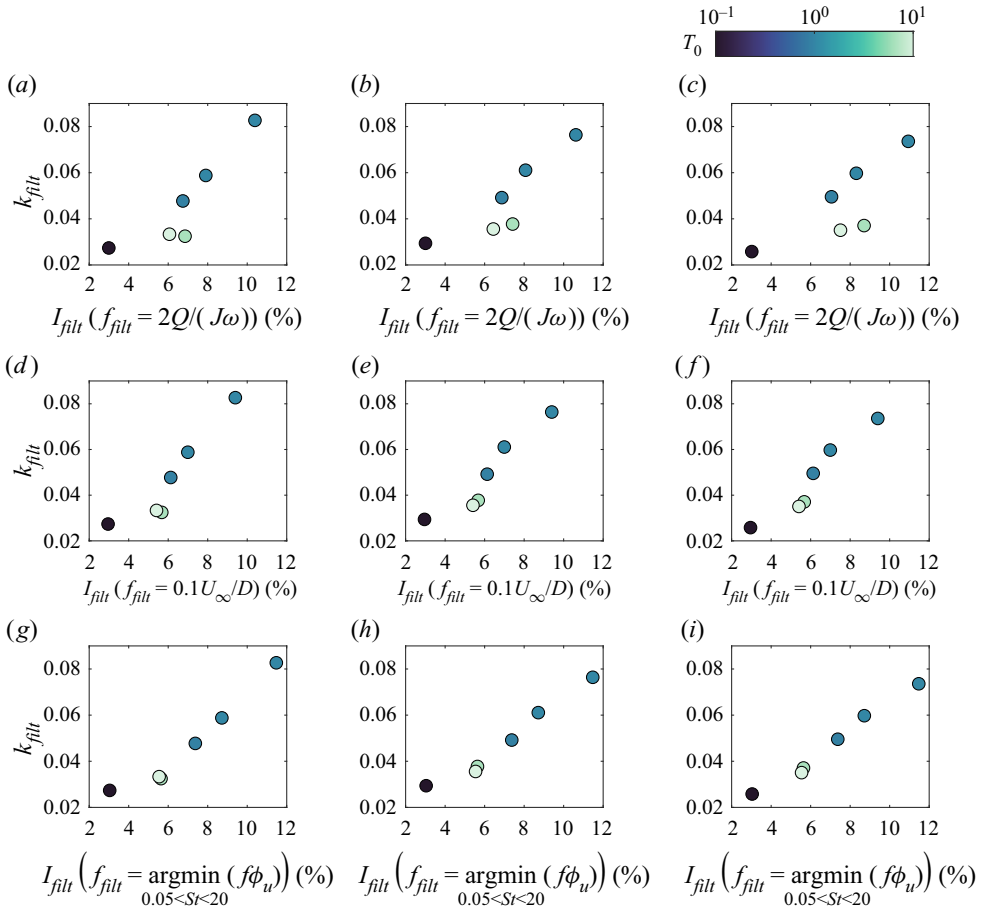
Figure 24. Trends of k_{filt} with the filtered turbulence intensity I_{filt}, for (a,d,g) $\lambda = 1.9$, (b,e,h) $\lambda = 3.8$ and (c,f,i) $\lambda = 4.7$, using three different definitions of f_{filt}.

4. Conclusions

This paper has presented measurements of the wake generated by a model-scale wind turbine in a streamwise plane for streamwise distances between $1.25D$ and $8.75D$ downstream of the rotor-swept plane. The free stream turbulence characteristics have been changed by means of an active grid to generate a variety of flows, of which some exhibited the canonical distribution of energy in the frequency domain of Kolmogorov, while others presented artificial contributions at very low frequencies; all flows have been defined by their free stream turbulence intensity I_∞ and their integral time scale T_0. For Kolmogorov-like flows, it has been seen that increasing the turbulence intensity in the free stream results in a wake whose evolution starts closer to the wind turbine rotor, whose recovery is faster and whose overall length is smaller, as shown in previous literature on wakes of both wind turbines and bluff bodies; highly turbulent inflows moreover induce more intense wake meandering. Wakes in non-Kolmogorov-like turbulence evolve more slowly, and their evolution starts further away from the turbine, than flows with equivalent or even smaller I_∞. Similarly, the amplitude of the wake meandering motion is reduced for these inflow conditions.

963 A19-32

To account for these differences, analytical wake models such as the widespread Gaussian wake model (Bastankhah & Porté-Agel 2014) must be reformulated as a function of two parameters: a virtual origin x_0 and a wake recovery rate k_{fit}. Results show here that k_{fit} varies considerably with the free stream turbulence conditions, while the wake diameter growth rate does not. With these assumptions, namely the presence of a virtual origin and the decoupling between the wake recovery rate and the wake diameter growth, the Gaussian wake model is excellent at predicting the minimum velocity in the wake. It has furthermore been observed that these two parameters refer to two different regions in the wake, as x_0 is broadly influenced by the near-wake length, while k_{fit} instead describes the flow behaviour in the far-wake.

In particular, the length of the near-wake has been estimated in this work by considerations on the turbulent kinetic energy distribution in the turbine wake: it has been observed that the near-wake length is small for high free stream turbulence intensity, and increases both with lower I_∞ and for non-Kolmogorov-like flows, following a trend similar to that of the virtual origin x_0. This trend is seen to be driven by the strength of the shear layer enveloping the wake: this is visualised as the instantaneous location of the tip-vortices shed by the turbine in its rotation, whose trajectories are considerably erratic for high-turbulence Kolmogorov inflows and more steady for low-I_∞ and non-Kolmogorov-like inflows. This change in the onset of shear-layer instability is the main driver of both the wake meandering observed in the far-wake and in the length of the near-wake. It has in fact been observed that wakes whose shear layers break up sooner are characterised, at the wake boundary, by intense sweep and ejection events, which favour the mixing between free stream and wake by expelling low-momentum flow from the wake and incorporating high-momentum flow from outside the wake. This behaviour is inhibited by long-lasting shear layers: these wakes have lower intensity of sweep and ejection events and higher intensity of interaction events, which are detrimental for the wake evolution. In particular, close to the wind turbine, the intensity of interaction events is the largest for the non-Kolmogorov-like flow at high I_∞ than any other wake here analysed.

The wake recovery rate in the far-wake is instead seen to be dominated by the Reynolds shear stress distribution at the wake centreline: it is seen that, for all wakes here investigated except the limit case of low I_∞ and high power, the analytical relationship $U(\partial U/\partial x) \simeq -2(\partial \overline{u'v'}/\partial y)$ holds true at the wake centreline. This relationship between the mean wake velocity and the in-plane Reynolds shear stress component has been leveraged to express an analytical relationship between the wake recovery rate k_{fit} and the distribution of Reynolds shear stress; experimental data show this relationship to hold true for the cases of high turbine thrust, while it is less accurate for the low-thrust test cases. Non-Kolmogorov-like flows are seen to result in slower-evolving wakes as these generate a lower value of Reynolds shear stress at the wake centreline: this behaviour is connected to the phenomenon for which the turbine is shown to harvest more power from the non-Kolmogorov-like flows, thus harvesting a larger fraction of the incoming turbulent kinetic energy from the free stream. This, in the literature, is seen as a bias of the turbulence spectra in the wake towards higher frequency contributions; in this work, this is shown as a large difference in the two-point correlation coefficient R_{uu} between free stream and wake for the non-Kolmogorov-like flow, a difference which is not evident for the classical Kolmogorov-like inflow conditions. Moreover, it has been shown that the linear trend between the wake recovery rate k_{fit} and the free stream turbulence intensity I_∞ can be recovered for the non-Kolmogorov-like flows if one excludes the contributions of low-frequency components from the computation of I_∞. In this work, this is shown by defining a filtered free stream turbulence intensity I_{filt} which is equivalent to I_∞

for canonical Kolmogorov inflows, and arbitrarily excludes low-frequency contributions for non-Kolmogorov-like flows; the trend if k_{fit} against I_{filt} is linear for all operating conditions analysed in this study. Results included in this work have also shown that an alternative definition of I_{filt}, in which all low-frequency contributions are filtered out of both Kolmogorov- and non-Kolmogorov-like inflows is not sufficient to recover the linear trend of k_{fit} with I_{filt}: this highlights how the wake behaviour is tied to the low-pass characteristics of the turbine when converting turbulent velocity fluctuations to mechanical power.

Author ORCIDs.

 Stefano Gambuzza https://orcid.org/0000-0001-9070-6901;

 Bharathram Ganapathisubramani https://orcid.org/0000-0001-9817-0486.

REFERENCES

AUBRUN, S., *et al.* 2019 Round-robin tests of porous disc models. *J. Phys.: Conf. Ser.* **1256**, 012004.

BARLAS, E., BUCKINGHAM, S. & VAN BEECK, J. 2016 Roughness effects on wind-turbine wake dynamics in a boundary-layer wind tunnel. *Boundary-Layer Meteorol.* **158** (1), 27–42.

BARTHELMIE, R., HANSEN, O.F., ENEVOLDSEN, K., HØJSTRUP, J., FRANDSEN, S., PRYOR, S., LARSEN, S., MOTTA, M. & SANDERHOFF, P. 2005 Ten years of meteorological measurements for offshore wind farms. *J. Sol. Energy Engng* **127** (2), 170–176.

BARTHELMIE, R.J. & JENSEN, L.E. 2010 Evaluation of wind farm efficiency and wind turbine wakes at the Nysted offshore wind farm. *Wind Energy* **13** (6), 573–586.

BASTANKHAH, M. & PORTÉ-AGEL, F. 2014 A new analytical model for wind-turbine wakes. *Renewable Energy* **70**, 116–123.

BLACKMORE, T., BATTEN, W.M.J., MÜLLER, G.U. & BAHAJ, A.S. 2014 Influence of turbulence on the drag of solid discs and turbine simulators in a water current. *Exp. Fluids* **55** (1), 1637.

CARBAJO FUERTES, F., MARKFORT, C.D. & PORTÉ-AGEL, F. 2018 Wind turbine wake characterization with nacelle-mounted wind lidars for analytical wake model validation. *Remote. Sens.* **10** (5), 668.

CASTRO, I. 1971 Wake characteristics of two-dimensional perforated plates normal to an air-stream. *J. Fluid Mech.* **46** (3), 599–609.

CHAMORRO, L.P., ARNDT, R.E.A. & SOTIROPOULOS, F. 2012 Reynolds number dependence of turbulence statistics in the wake of wind turbines. *Wind Energy* **15** (5), 733–742.

CHAMORRO, L.P., LEE, S.-J., OLSEN, D., MILLIREN, C., MARR, J., ARNDT, R.E.A. & SOTIROPOULOS, F. 2015 Turbulence effects on a full-scale 2.5 MW horizontal-axis wind turbine under neutrally stratified conditions. *Wind Energy* **18** (2), 339–349.

CHAMORRO, L.P. & PORTÉ-AGEL, F. 2009 A wind-tunnel investigation of wind-turbine wakes: boundary-layer turbulence effects. *Boundary-Layer Meteorol.* **132** (1), 129–149.

CHAMORRO, L.P. & PORTÉ-AGEL, F. 2010 Effects of thermal stability and incoming boundary-layer flow characteristics on wind-turbine wakes: A wind-tunnel study. *Boundary-Layer Meteorol.* **136** (3), 515–533.

CHATTERJEE, T. & PEET, Y.T. 2018 Contribution of large scale coherence to wind turbine power: A large eddy simulation study in periodic wind farms. *Phys. Rev. Fluids* **3** (3), 034601.

CHATTERJEE, T. & PEET, Y.T. 2021 Streamwise inhomogeneity of spectra and vertical coherence of turbulent motions in a finite-size wind farm. *Phys. Rev. Fluids* **6** (11), 114601.

CHRISTENSEN, K.T. 2004 The influence of peak-locking errors on turbulence statistics computed from PIV ensembles. *Exp. Fluids* **36** (3), 484–497.

CHRISTIANSEN, M.B. & HASAGER, C.B. 2005 Wake effects of large offshore wind farms identified from satellite SAR. *Remote Sens. Environ.* **98** (2), 251–268.

CRESPO, A. & HERNÁNDEZ, J. 1996 Turbulence characteristics in wind-turbine wakes. *J. Wind Engng Ind. Aerodyn.* **61** (1), 71–85.

DASARI, T., WU, Y., LIU, Y. & HONG, J. 2019 Near-wake behaviour of a utility-scale wind turbine. *J. Fluid Mech.* **859**, 204–246.

DE CILLIS, G., CHERUBINI, S., SEMERARO, O., LEONARDI, S. & DE PALMA, P. 2020 POD-based analysis of a wind turbine wake under the influence of tower and nacelle. *Wind Energy* **24**, 609–633.

DESKOS, G., PAYNE, G.S. & GAURIER, B. 2020 On the spectral behaviour of the turbulence-driven power fluctuations of horizontal-axis turbines. *J. Fluid Mech.* **904** (A13), 13–14.

DOGAN, E., HANSON, R.E. & GANAPATHISUBRAMANI, B. 2016 Interactions of large-scale free-stream turbulence with turbulent boundary layers. *J. Fluid Mech.* **802**, 79–107.

ELLIOTT, D. & CADOGAN, J. 1990 Effects of wind shear and turbulence on wind turbine power curves. In *Proceedings of the 1990 European Community Wind Energy Conference and Exhibition* (ed. W. Palz). H. S. Stephens.

ESPAÑA, G., AUBRUN, S., LOYER, S. & DEVINANT, P. 2011 Spatial study of the wake meandering using modelled wind turbines in a wind tunnel. *Wind Energy* **14** (7), 923–937.

FOTI, D., YANG, X., CAMPAGNOLO, F., MANIACI, D. & SOTIROPOULOS, F. 2018 Wake meandering of a model wind turbine operating in two different regimes. *Phys. Rev. Fluids* **3** (5), 054607.

FOTI, D., YANG, X., SHEN, L. & SOTIROPOULOS, F. 2019 Effect of wind turbine nacelle on turbine wake dynamics in large wind farms. *J. Fluid Mech.* **869**, 1–26.

FRANDSEN, S. & BARTHELMIE, R. 2002 Local wind climate within and downwind of large offshore wind turbine clusters. *Wind Engng* **26** (1), 51–58.

FRANDSEN, S., BARTHELMIE, R.J., PRYOR, S., RATHMANN, O., LARSEN, S., HØJSTRUP, J. & THØGERSEN, M. 2006 Analytical modelling of wind speed deficit in large offshore wind farms. *Wind Energy* **9** (1–2), 39–53.

GAMBUZZA, S. & GANAPATHISUBRAMANI, B. 2021 The effects of free-stream turbulence on the performance of a model wind turbine. *J. Renewable Sustainable Energy* **13** (2), 023304.

HALLER, G. 2005 An objective definition of a vortex. *J. Fluid Mech.* **525**, 1–26.

HEARST, R. & GANAPATHISUBRAMANI, B. 2015 Quantification and adjustment of pixel-locking in particle image velocimetry. *Exp. Fluids* **56** (10), 191.

HEARST, R. & GANAPATHISUBRAMANI, B. 2017 Tailoring incoming shear and turbulence profiles for lab-scale wind turbines. *Wind Energy* **20** (12), 2021–2035.

HEARST, R.J., GOMIT, G. & GANAPATHISUBRAMANI, B. 2016 Effect of turbulence on the wake of a wall-mounted cube. *J. Fluid Mech.* **804**, 513–530.

HEARST, R.J. & LAVOIE, P. 2016 Effects of multi-scale and regular grid geometries on decaying turbulence. *J. Fluid Mech.* **803**, 528–555.

HEISEL, M., HONG, J. & GUALA, M. 2018 The spectral signature of wind turbine wake meandering: A wind tunnel and field-scale study. *Wind Energy* **21** (9), 715–731.

DER HOVEN, I.V. 1957 Power spectrum of horizontal wind speed in the frequency range from 0.0007 to 900 cycles per hour. *J. Atmos. Sci.* **14** (2), 160–164.

HOWARD, K.B., SINGH, A., SOTIROPOULOS, F. & GUALA, M. 2015 On the statistics of wind turbine wake meandering: an experimental investigation. *Phys. Fluids* **27** (7), 075103.

HUNT, J.C.R., WRAY, A.A. & MOIN, P. 1988 Eddies, streams, and convergence zones in turbulent flows. *Rep. No.* CTR-S88, pp. 193–208. Center for Turbulence Research.

ISHIHARA, T. & QIAN, G.W. 2018 A new Gaussian-based analytical wake model for wind turbines considering ambient turbulence intensities and thrust coefficient effects. *J. Wind Engng Ind. Aerodyn.* **177**, 275–292.

IVANELL, S., MIKKELSEN, R., SØRENSEN, J.N. & HENNINGSON, D. 2010 Stability analysis of the tip vortices of a wind turbine. *Wind Energy* **13** (8), 705–715.

JENSEN, N. 1983 *A Note on Wind Generator Interaction*. Risø National Laboratory.

JEONG, J. & HUSSAIN, F. 1995 On the identification of a vortex. *J. Fluid Mech.* **285**, 69–94.

KANG, S., YANG, X. & SOTIROPOULOS, F. 2014 On the onset of wake meandering for an axial flow turbine in a turbulent open channel flow. *J. Fluid Mech.* **744**, 376–403.

KISTLER, A.L. & VREBALOVICH, T. 1966 Grid turbulence at large Reynolds numbers. *J. Fluid Mech.* **26** (1), 37–47.

KOLMOGOROV, A.N. 1941 The local structure of turbulence in incompressible viscous fluid for very large Reynolds numbers. *Dokl. Akad. Nauk SSSR.* **30**, 301.

LI, Z., DONG, G. & YANG, X. 2022 Onset of wake meandering for a floating offshore wind turbine under side-to-side motion. *J. Fluid Mech.* **934**, A29.

LI, L., HEARST, R., FERREIRA, M. & GANAPATHISUBRAMANI, B. 2020 The near-field of a lab-scale wind turbine in tailored turbulent shear flows. *Renewable Energy* **149**, 735–748.

LIGNAROLO, L., RAGNI, D., KRISHNASWAMI, C., CHEN, Q., SIMÃO FERREIRA, C. & VAN BUSSEL, G. 2014 Experimental analysis of the wake of a horizontal-axis wind-turbine model. *Renewable Energy* **70**, 31–46.

LIGNAROLO, L.E.M., RAGNI, D., SCARANO, F., SIMÃO FERREIRA, C.J. & VAN BUSSEL, G.J.W. 2015 Tip-vortex instability and turbulent mixing in wind-turbine wakes. *J. Fluid Mech.* **781**, 467–493.

LISSAMAN, P.B.S. 1979 Energy effectiveness of arbitrary arrays of wind turbines. *J. Energy* **3** (6), 323–328.

MAKITA, H. 1991 Realization of a large-scale turbulence field in a small wind tunnel. *Fluid Dyn. Res.* **8**, 53–64.

MEDICI, D. & ALFREDSSON, P.H. 2006 Measurements on a wind turbine wake: 3D effects and bluff body vortex shedding. *Wind Energy* **9** (3), 219–236.

MONIN, A.S. & OBUKHOV, A.M. 1954 Basic laws of turbulent mixing in the surface layer of the atmosphere. *Contrib. Geophys. Inst. Acad. Sci. USSR* **151** (163), 163–187.

MYCEK, P., GAURIER, B., GERMAIN, G., PINON, G. & RIVOALEN, E. 2014 Experimental study of the turbulence intensity effects on marine current turbines behaviour. Part I: one single turbine. *Renewable Energy* **66**, 729–746.

NEUNABER, I., HÖLLING, M., STEVENS, R.J.A.M., SCHEPERS, G. & PEINKE, J. 2020 Distinct turbulent regions in the wake of a wind turbine and their inflow-dependent locations: the creation of a wake map. *Energies* **13** (20), 5392.

NEUNABER, I., HÖLLING, M., WHALE, J. & PEINKE, J. 2021 Comparison of the turbulence in the wakes of an actuator disc and a model wind turbine by higher order statistics: A wind tunnel study. *Renewable Energy* **179**, 1650–1662.

NEUNABER, I., PEINKE, J. & OBLIGADO, M. 2022 Application of the Townsend–George theory for free shear flows to single and double wind turbine wakes – a wind tunnel study. *Wind Energy Sci.* **7** (1), 201–219.

NIAYIFAR, A. & PORTÉ-AGEL, F. 2016 Analytical modeling of wind farms: a new approach for power prediction. *Energies* **9** (9), 741.

PAL, A. & SARKAR, S. 2015 Effect of external turbulence on the evolution of a wake in stratified and unstratified environments. *J. Fluid Mech.* **772**, 361–385.

PEÑA, A., FLOORS, R., SATHE, A., GRYNING, S.-E., WAGNER, R., COURTNEY, M.S., LARSÉN, X.G., HAHMANN, A.N. & HASAGER, C.B. 2016 Ten years of boundary-layer and wind-power meteorology at Høvsøre, Denmark. *Boundary-Layer Meteorol.* **158** (1), 1–26.

POORTE, R.E. & BIESHEUVEL, A. 2002 Experiments on the motion of gas bubbles in turbulence generated by an active grid. *J. Fluid Mech.* **461**, 127–154.

POPE, S.B. 2000 *Turbulent Flows*. Cambridge University Press.

POPE, S.B. & WHITELAW, J.H. 1976 The calculation of near-wake flows. *J. Fluid Mech.* **73** (1), 9–32.

RIND, E. & CASTRO, I.P. 2012*a* On the effects of free-stream turbulence on axisymmetric disc wakes. *Exp. Fluids* **53** (2), 301–318.

RIND, E. & CASTRO, I.P. 2012*b* Direct numerical simulation of axisymmetric wakes embedded in turbulence. *J. Fluid Mech.* **710**, 482–504.

SAKAMOTO, H. & ARIE, M. 1983 Vortex shedding from a rectangular prism and a circular cylinder placed vertically in a turbulent boundary layer. *J. Fluid Mech.* **126**, 147–165.

SARMAST, S., DADFAR, R., MIKKELSEN, R.F., SCHLATTER, P., IVANELL, S., SØRENSEN, J.N. & HENNINGSON, D.S. 2014 Mutual inductance instability of the tip vortices behind a wind turbine. *J. Fluid Mech.* **755**, 705–731.

SHARP, N.S., NEUSCAMMAN, S. & WARHAFT, Z. 2009 Effects of large-scale free stream turbulence on a turbulent boundary layer. *Phys. Fluids* **21** (9), 095105.

SHEINMAN, Y. & ROSEN, A. 1992 A dynamic model of the influence of turbulence on the power output of a wind turbine. *J. Wind Engng Ind. Aerodyn.* **39** (1–3), 329–341.

SMEDMAN-HÖGSTRÖM, A.-S. & HÖGSTRÖM, U. 1975 Spectral gap in surface-layer measurements. *J. Atmos. Sci.* **32** (2), 340–350.

SØRENSEN, J.N., MIKKELSEN, R.F., HENNINGSON, D.S., IVANELL, S., SARMAST, S. & ANDERSEN, S.J. 2015 Simulation of wind turbine wakes using the actuator line technique. *Phil. Trans. R. Soc. Lond.* A **373** (2035), 20140071.

SPEDDING, G.R., BROWAND, F.K. & FINCHAM, A.M. 1996 Turbulence, similarity scaling and vortex geometry in the wake of a towed sphere in a stably stratified fluid. *J. Fluid Mech.* **314**, 53–103.

TENNEKES, H. & LUMLEY, J.L. 1972 *A First Course in Turbulence*. MIT Press.

TOBIN, N. & CHAMORRO, L.P. 2019 Modulation of turbulence scales passing through the rotor of a wind turbine. *J. Turbul.* **20** (1), 21–31.

TOBIN, N., ZHU, H. & CHAMORRO, L.P. 2015 Spectral behaviour of the turbulence-driven power fluctuations of wind turbines. *J. Turbul.* **16** (9), 832–846.

TOWNSEND, A.A. 1999 *The Structure of Turbulent Shear Flow*. Cambridge Monographs on Mechanics and Applied Mathematics, 2nd edn. Cambridge University Press.

TROLDBORG, N., SORENSEN, J.N. & MIKKELSEN, R. 2010 Numerical simulations of wake characteristics of a wind turbine in uniform inflow. *Wind Energy* **13** (1), 86–99.

TÜRK, M. & EMEIS, S. 2010 The dependence of offshore turbulence intensity on wind speed. *J. Wind Engng Ind. Aerodyn.* **98** (8), 466–471.

UBEROI, M.S. & FREYMUTH, P. 1970 Turbulent energy balance and spectra of the axisymmetric wake. *Phys. Fluids* **13** (9), 2205–2210.

VERMEER, L., SØRENSEN, J. & CRESPO, A. 2003 Wind turbine wake aerodynamics. *Prog. Aerosp. Sci.* **39** (6–7), 467–510.

VINNES, M.K., GAMBUZZA, S., GANAPATHISUBRAMANI, B. & HEARST, R.J. 2022 The far wake of porous disks and a model wind turbine: similarities and differences assessed by hot-wire anemometry. *J. Renewable Sustainable Energy* **14** (2), 023304.

WAGNER, R., COURTNEY, M., GOTTSCHALL, J. & LINDELÖW-MARSDEN, P. 2011 Accounting for the speed shear in wind turbine power performance measurement. *Wind Energy* **14** (8), 993–1004.

WIENEKE, B. 2015 PIV uncertainty quantification from correlation statistics. *Meas. Sci. Technol.* **26** (7), 074002.

WU, Y.-T. & PORTÉ-AGEL, F. 2012 Atmospheric turbulence effects on wind-turbine wakes: an LES study. *Energies* **5** (12), 5340–5362.

WYGNANSKI, I., CHAMPAGNE, F. & MARASLI, B. 1986 On the large-scale structures in two-dimensional, small-deficit, turbulent wakes. *J. Fluid Mech.* **168** (−1), 31.

ZHANG, W., MARKFORT, C.D. & PORTÉ-AGEL, F. 2013 Wind-turbine wakes in a convective boundary layer: a wind-tunnel study. *Boundary-Layer Meteorol.* **146** (2), 161–179.